Predictions for Micro- and Macroturbulence as function of the Mixing-Length Parameter in inflated massive main sequence stars

Bachelorarbeit in Physik von Katharina Rauthmann

angefertigt am
Argelander-Institut für Astronomie

vorgelegt der
Mathematisch-Naturwissenschaftlichen Fakultät

der
Rheinischen Friedrich-Wilhelms-Universität Bonn

März 2016

1. Gutachter: Prof. Dr. Norbert Langer
2. Gutachter: Dr. Richard Stancliffe

Abstract

The partial ionisation of helium and iron in the envelopes of massive main sequence stars induce extended sub-surface convection zones. In this thesis, the properties and observable consequences regarding macro- and microturbulence of the convection zones are investigated for stellar models with $60M_{\odot}$ and a set of different mixing-length parameters using the stellar evolution code BEC.

We find that larger mixing-length parameters suppress envelope inflation and cause higher turbulent pressure fractions and convective velocities. The parameter $\alpha = 2$ is established as a transitional value, above which the properties of the convection zones are altered significantly. We also find that neither models with very small ($\alpha = 0.5$) nor very large ($\alpha \geq 3$) can explain the observations regarding macro- and microturbulence.

Contents

1 Introduction

The evolution of massive stars is still not well understood, even on the main sequence, despite their importance in enriching the interstellar medium, as producers of powerful stellar winds and as possible progenitors of different types of supernovae and long-duration gamma-ray bursts. In particular, many questions remain regarding the process of convection and its effects on various phenomena in high-mass stars. The Mixing Length Theory (Böhm-Vitense 1958) is commonly used to describe convection, but is expected to have shortcomings particularly for stars reaching or even exceeding the Eddington limit (Sanyal et al. 2015). Massive stars are commonly understood to possess a convective core and a radiative envelope. However, the introduction of helium and iron opacity peaks due to partial ionisation in models for stellar opacities (Iglesias et al. 1992) has led to predictions of extended sub-surface convection zones in massive stars.

Previous studies have investigated the presence of turbulent motions in the outer layers of massive stars as possible causes for observations of both macroturbulence and microturbulence (see Cantiello et al. 2009, Grassitelli et al. 2015). So far, these examinations assumed one fixed mixing-length parameter in describing convection, which is a free parameter in the Mixing Length Theory however and not known a priori. Therefore it is useful to create models of stellar evolution with different sets of mixing-length parameters and compare these with observations in order to better understand the processes in massive stars. It is the aim of this thesis to investigate how the properties and behaviour of sub-surface convection zones in a $60 M_{\odot}$ star as well as their observable consequences are influenced by the mixing-length parameter in the framework of the Mixing-Length Theory.

In the second Section, an overview about the current understanding of convection and a description of the stellar models used in this thesis will be given. In Sect. 3, we will compare models with slightly different masses and investigate how the mixing-length parameter influences the phenomenon of envelope inflation. Section 4 contains examinations about the strength of convective motions and the turbulent pressure in sub-surface convection zones. We also try to find a connection to macroturbulence (Grassitelli et al. 2015) and determine whether observations help in calibrating the mixing-length parameter. Lastly, in Sect. 5, we will investigate how different mixing-length parameters would change the results for microturbulence, as examined in Cantiello et al. (2009).

2 Theoretical background and the stellar models

Convection in the framework of the Mixing Length Theory

The mixing length theory (called MLT hereafter) is a simple one-dimensional, yet successful description of convection proposed by Ludwig Prandtl (1925). Convection is an energy transport mechanism involving the motion of blobs of gas with either excess heat or a heat deficit travelling radially upwards or downwards in the convection zone. The travel distance over which the gas blobs release or absorb heat before dissolving into their surroundings is the so called mixing length l, which is defined as (Pols 2009):

$$l = \alpha H_{\mathrm{P}} \ , \tag{1}$$

where H_{P} is the pressure scale height

$$H_{\mathrm{P}} = \left| \frac{dr}{dlnP} \right| = \frac{P}{\rho g} = \frac{P \cdot R^2}{\rho \cdot GM} \tag{2}$$

where $P = P_g + P_r$ is the total pressure. The mixing-length parameter α is a free parameter which has to be calibrated.

The convective velocity v_{c} is dependent on the superadiabaticity $\nabla - \nabla_{\mathrm{ad}}$, where ∇ is the actual and ∇_{ad} the adiabatic temperature gradient. It can be approximated as (Pols)

$$v_{\mathrm{c}} \approx \sqrt{\frac{l_{\mathrm{m}}^2 g}{2H_{\mathrm{P}}} \cdot (\nabla - \nabla_{\mathrm{ad}})} \ , \tag{3}$$

from which follows that $v_{\mathrm{c}} \propto \alpha\sqrt{H_{\mathrm{P}}}$.

Significance of convection zones in the envelopes of massive stars

Generally, massive stars are expected to have convective cores and radiative envelopes (Pols 2009). However, there are opacity peaks (or 'bumps') due to the partial ionisation of iron and helium predicted at $log(T) \approx 5.3$ and $log(T) \approx 4.6$ respectively (Iglesias et al. 1992). In stellar layers with corresponding temperatures, these opacity peaks induce convection zones in the stellar envelope close to the surface. For the stellar mass analysed in this thesis, $60 M_{\odot}$ with galactic metallicity, the convection zone caused by the iron opacity peak (called FeCZ hereafter) is present throughout the main sequence evolution. The helium convection zone (HeCZ hereafter) on the other hand only emerges once the effective temperature T_{eff} has decreased sufficiently. The convection zones do not affect the stellar structure significantly, but they are predicted to produce observable phenomena on the surface of stars, namely microturbulence and macroturbulence (Cantiello et al. 2009, Grassitelli et al. 2015). Additionally, iron creates a second opacity peak, which is located significantly deeper in the envelope, at $log(T) \approx 6.2$, which can not cause macro- or microturbulence since the peak has a relatively low strength and is located at a high optical depth.

Macroturbulence

Spectral lines of massive stars are broadened mainly by rotation, although it can not account for all observed line-broadening. The spectra of OB stars are expected to be affected by macroturbulent broadening, which is an extra line-broadening associated with large scale surface motions (large compared to the line forming region; Grassitelli et al. 2015). Convection in the convection zones close to the surface is suspected to be involved in the origin of macroturbulence. As convective velocities approach the isothermal sound speed

$$c_{\mathrm{s,iso}} = \sqrt{\frac{k_{\mathrm{B}} T}{\mu m_{\mathrm{H}}}} = \sqrt{\frac{P_{\mathrm{g}}}{\rho}} \tag{4}$$

(where k_{B} is the Boltzmann constant, T is the local temperature, μ is the mean molecular weight, m_H is the proton mass and P_{g} is the local gas pressure), the MLT may be insufficient to describe convection as the turbulent pressure and dissipative effects become significant, which may be the cause of macroturbulence. The turbulent pressure is defined as (Grassitelli et al. 2015)

$$P_{\mathrm{turb}} = \frac{1}{3} \rho v_{\mathrm{c}}^2 \ , \tag{5}$$

where ρ is the local gas density and v_{c} is the local convective velocity. This equation assumes isotropic turbulence.

Microturbulence

There is another possible extra line-broadening in the spectra of OB stars. The upper part of a convection zone, due to the interactions with the overlying radiative layers, can generate acoustic and gravity waves, which propagate outward. When they reach the surface, small scale velocity fluctuations are induced, called microturbulence (Cantiello

et al. 2009). The crucial parameter for these surface velocity fluctuations is the average convective velocity in the last mixing length of the convective zone, defined in Cantiello et al. (2009) as

$$\langle v_{\rm c} \rangle = \frac{1}{\alpha H_{\rm P}} \int_{R_{\rm c}-\alpha H_{\rm P}}^{R_{\rm c}} v_{\rm c}(r) dr \quad , \tag{6}$$

where $R_{\rm c}$ is the upper boundary of the CZ and $v_{\rm c}(r)$ is the local convective velocity. From this, only considering energy transport through gravity waves, Cantiello et al. (2009) found an upper limit for the expected velocity amplitudes at the stellar surface of

$$v_{\rm s} \leq \langle v_{\rm c} \rangle \sqrt{M_{\rm c} \frac{\rho_{\rm c}}{\rho_{\rm s}}} \quad , \tag{7}$$

where $M_{\rm c}$ is the isothermal Mach number at the upper boundary of the CZ (Sanyal et al. 2015):

$$M_{\rm c} = \frac{v_{\rm c}}{c_{\rm s,iso}} \quad , \tag{8}$$

with $c_{\rm s,iso}$ as the local isothermal sound speed. With observed Doppler widths in photospheric absorption lines of (Cantiello et al. 2009)

$$\Delta\lambda_{\rm D} = \frac{\lambda}{c} \sqrt{\frac{2\mathcal{R}T}{\mu} + \xi^2} \quad , \tag{9}$$

the microturbulent velocity ξ can be determined.

2.1 Stellar models

To examine the various effects of convection in massive stars, one single star model with $60 M_\odot$ initial mass, no rotation and solar initial composition is used to compute the evolution of stars with several different mixing-length parameters, namely $\alpha = 0.5, 1.5, 2.0, 3.0, 5.0, 30.0$. The models are computed with the Lagrangian one-dimensional hydrodynamic stellar evolution code BEC, which treats convection according to the Mixing-Length Theory (MLT). The same parameters as in Brott et al. (2011) are used, except for the mixing-length parameters α, which is varied. The opacity of stellar matter is taken from OPAL opacity table (Iglesias & Rogers 1996). Mass-loss by stellar wind is taken into account according to Vink et al. (2001). For $\alpha = 0.5$, an additional model was computed, setting the initial mass to $62 M_\odot$ instead, to produce a model with luminosity values closer to those of different mixing-length parameter values (see Figure 1 and Sect. 3.1).

Although the examination of the behaviour of the turbulent pressure is an aim of this thesis, the stellar models were computed without a modification to the BEC in order to include turbulent terms (see Grassitelli et al. 2015). Instead the turbulent pressure is calculated a posteriori using Eq. 5. This method should still result in useful models because regions containing high turbulent pressure contain very little mass (Grassitelli et al.). Therefore evolutionary tracks do not differ significantly whether turbulent pressure is included in the stellar code or not.

In the analysis we limit the convective velocity $v_{\rm c}$ to the local isothermal sound speed, $c_{\rm s,iso}$, i.e.

$$v_{\rm c} \leq c_{\rm s,iso} \quad , \tag{10}$$

which is calculated according to Eq. 4. This is done because supersonic convective velocities are outside the frame of the MLT and may be unrealistic (Sanyal et al. 2015). As a consequence, the turbulent pressure is limited by this condition as well, meaning that $P_{\rm turb}$ in these models cannot exceed one third of the local gas pressure.

This thesis focuses on three effective temperatures for examining the properties of the stellar models. They were chosen to be $T_{\rm eff} = 40$kK, $T_{\rm eff} = 25$kK and $T_{\rm eff} = 15$kK, in order to cover the early, middle and late main sequence of the models. To compare models with approximately the same $T_{\rm eff}$, for each mixing-length parameter the model closest to a specific temperatures is chosen. The computation of both models with the mixing-length parameter $\alpha = 0.5$ could not continue past the temperatures seen in Figures 1 and 2. Therefore at $T_{\rm eff} = 15$kK only models of $\alpha \geq 1.5$ can be analysed.

3 Properties of the investigated models

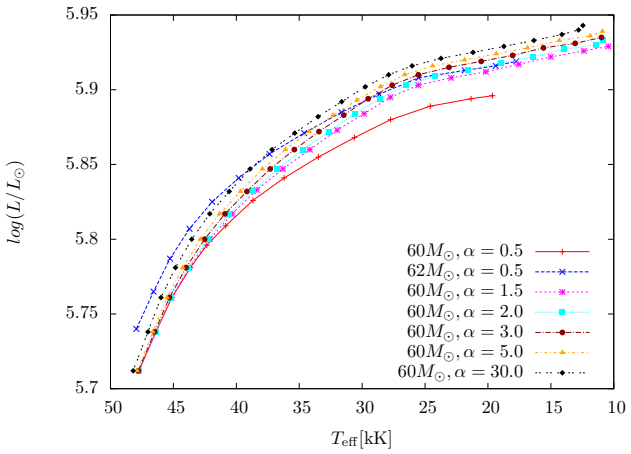

Figure 1: HRD with evolutionary tracks of main sequence stellar models with different mixing-length parameters α. Shown are tracks for initial masses of $60M_\odot$ with six different values for α and an additional track with an initial mass of $62M_\odot$ with a mixing-length parameter of $\alpha = 0.5$. Dots indicate the models for each mixing-length parameter that can be investigated further. The track with an initial mass of $60M_\odot$ and a mixing-length parameters of $\alpha = 1.5$ corresponds to the track for $60M_\odot$ by Brott et al. (2011)

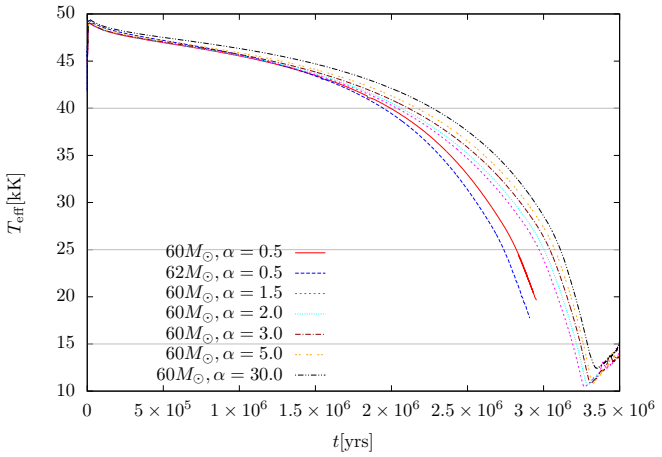

Figure 2: Behaviour of the effective temperature $T_{\rm eff}$ over time for stellar models with an initial mass of $60M_\odot >$ with different mixing-length parameters α and a stellar model with initial mass $62M_\odot$ and $\alpha = 0.5$. The lines at $T_{\rm eff} = 40$kK, 25kK and 15kK indicate the effective temperatures at which the properties of the stellar models will be investigated in this thesis.

Figure 1 shows the Hertzsprung-Russell diagram (HRD) of the main sequence models for a set of mixing-length parameters. The evolutionary tracks of the stellar models in the HRD are similar for the different mixing-length parameters. However, the larger α, the higher the effective temperature $T_{\rm eff}$ of models with the same luminosity L. Luminosity is only influenced by mass and chemical composition, the apparent discrepancy in the stellar tracks for models of different mixing-length parameters therefore stems from $T_{\rm eff}$. Convection creates a net heat flux upwards as gas blobs are transported up and down. In convective zones close to the surface, as the HeCZ and FeCZ discussed in this thesis, the heat flux creates a significant increase in the surface temperature, which is stronger for larger mixing-length parameters. For $\alpha = 0.5$, the mixing length is very small, which creates a considerable discrepancy in temperature from other models in the HRD. Further examinations will concentrate on models of different mixing-length parameters with the same effective temperature, to facilitate comparison with other studies using fixed effective temperatures. These models still have similar luminosities. Only for the models with $\alpha = 0.5$ the difference in luminosity is significant. Therefore a stellar model using $\alpha = 0.5$ with a slightly higher mass of $62M_\odot$ was computed, which is also shown in Figure 1. For these models, luminosities at a certain $T_{\rm eff}$ are closer to luminosities of models with larger mixing-length parameters.

Figure 2 shows how the effective temperature changes over time on the main sequence. The higher the mixing-length parameter, the higher is $T_{\rm eff}$ at a particular time, as expected due to convection increasing the surface temperature. Convection is also a mixing mechanism, therefore the lifetime on the main sequence is slightly increased for larger mixing-length parameters, as hydrogen is mixed into the regions of nuclear burning. This happens in the core of the stellar models however, and the HeCZ and FeCZ are close to the surface. This aspect will therefore not be investigated further in this thesis. The first step is to determine whether the models for $\alpha = 0.5$ at $60M_\odot$ and $62M_\odot$ are similar enough so that the $62M_\odot$ model can be used to compare stellar models using different mixing-length parameters.

3.1 Comparison of the $60M_\odot$ and $62M_\odot$ models with $\alpha = 0.5$

To determine whether the model with an initial mass of $62M_\odot$ and a mixing-length parameter of $\alpha = 0.5$ can be compared and used instead of the model with an initial mass of $60M_\odot$ and $\alpha = 0.5$, their properties and the behaviour of convective velocities and turbulent pressure at $T_{\rm eff} = 40kK$ and $T_{\rm eff} = 25kK$ are shown in Table 1 and Figures 3 - 6.

Table 1 shows the age, current mass, luminosity, effective temperature and radius. Important to note is that the models used do not have effective temperatures of exactly 40kK or 25kK, instead these are the two models each with effective temperatures closest to 40kK and 25kK. As shown in Figure 2, the effective temperature of the $62M_\odot$ model decreases more quickly than that of the $60M_\odot$ model due to its higher mass, which means a slightly shorter lifetime on the main sequence. The overall behaviour is similar, as are the evolutionary tracks in Figure 1 for both models, which differ only in luminosity.

Table 1: Stellar properties of the models near $T_{\rm eff} = 40$kK and $T_{\rm eff} = 25$kK with a mixing-length parameter of $\alpha = 0.5$ for the initial masses $60M_\odot$ and $62M_\odot$. Shown are the models' ages, current masses, luminosities, effective temperatures and radii.

Model referenced as:	$60M_\odot$, 40kK	$62M_\odot$, 40kK	$60M_\odot$, 25 kK	$62M_\odot$, 25 kK
t in yrs	1.90×10^6	1.96×10^6	2.83×10^6	2.72×10^6
$M/M_\odot$	55.3634	56.6586	52.0164	53.8991
$log(L/L_\odot)$	5.809	5.841	5.889	5.908
$T_{\rm eff}/K$	40842	39805	24581	25513
$R/R_\odot$	16.0355	17.5145	48.5384	46.0296

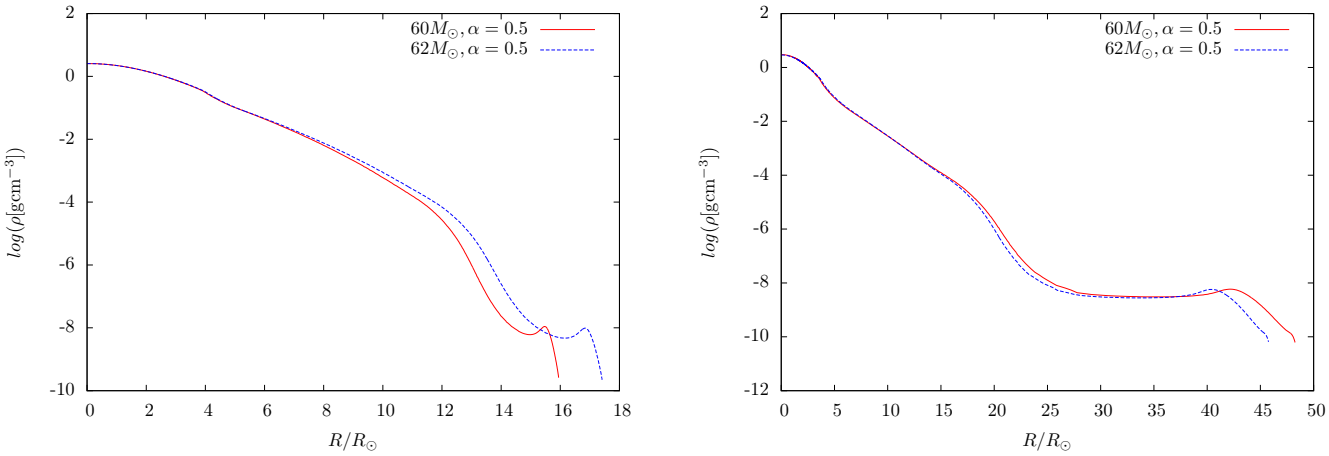

Figure 3: Density ρ as a function of stellar radius R for two models with initial masses of $60M_\odot$ and $62M_\odot$, with a mixing-length parameter of $\alpha = 0.5$. Left panel: Models at an effective temperature of $T_{\rm eff} = 40$kK, showing a clear density inversion and inflation in the stellar envelope. Right panel: Models at $T_{\rm eff} = 25$kK, showing that the density inversion still exists and that strength of inflation has increased significantly.

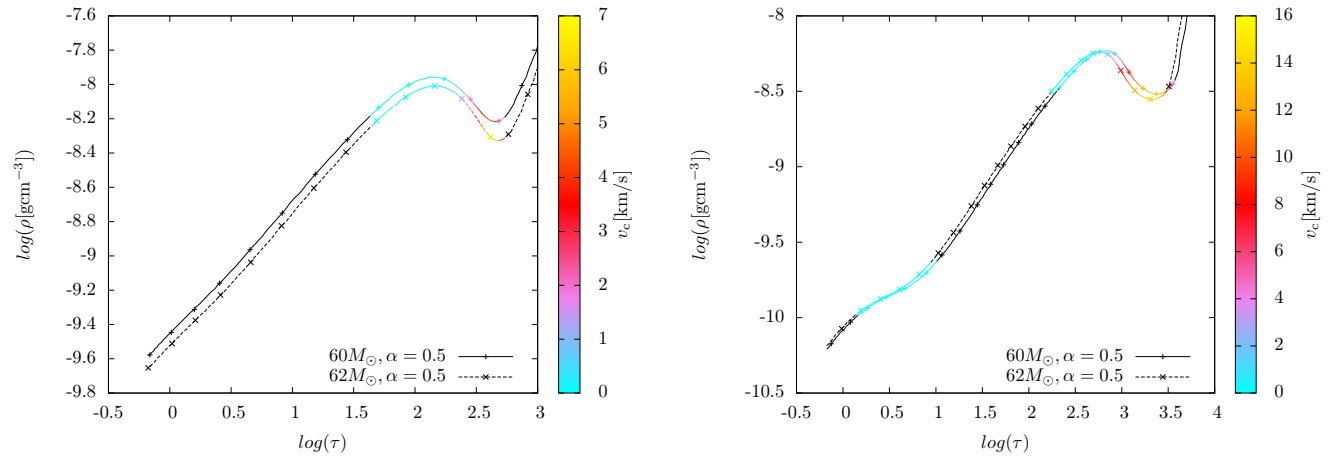

Figure 4: Convective velocities v_c (colour-coded) as a function of density ρ and optical depth τ for stellar models with initial masses of $60M_\odot$ and $62M_\odot$ and a mixing-length parameter $\alpha = 0.5$. Not all calculated grid points are shown. Regions with $v_c \simeq 0$ are coloured black to indicate the extent of convection zones. Convection zones at these optical depths occur due to the iron opacity peak at $log(T) \approx 5.3$ and the helium opacity peak at $log(T) \approx 4.6$. Left panel: Models at $T_{\rm eff} = 40$kK, showing convective velocities as well as the optical depth and extent of the FeCZ. It is shown that the density inversion seen in Fig. 3 occurs in the FeCZ. Right panel: Convective velocities as well as the optical depth and extent of the HeCZ and FeCZ for models at $T_{\rm eff} = 25$kK. The FeCZ causes the density inversion and in the HeCZ the density increases less steeply.

The density profiles for the chosen effective temperatures are shown in Fig. 3. The behaviour of both models is very similar, including the expected density inversions and inflation (see Sect. 3.2). The actual radius is not identical, which is due to several factors. Generally main sequence stars follow the mass-radius relation of $R \propto M^{0.7}$ (Pols 2009), causing the $62M_\odot$ model to have a slightly higher radius at the same effective temperature, which is the main factor at $T_{\rm eff} = 40$kK, where inflation is not yet strong. At $T_{\rm eff} = 25$kK inflation is very pronounced. The $60M_\odot$ model has a slightly lower temperature (see Table 1), which is cause for the higher radius. Since the overall behaviour for both

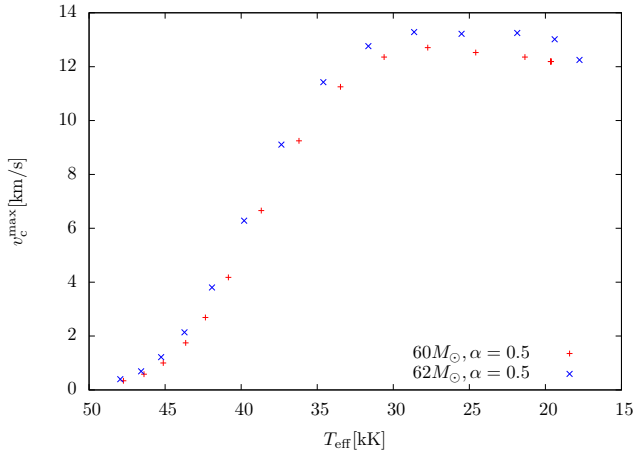

Figure 5: Behaviour of the maximum convective velocity v_c during the main sequence as a function of T_{eff} for models with initial masses of $60M_\odot$ and $62M_\odot$ with a mixing-length parameter of $\alpha = 0.5$.

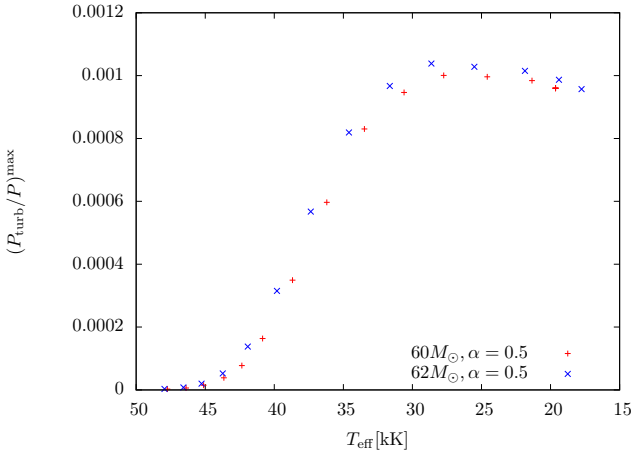

Figure 6: Behaviour of the maximum turbulent pressure fraction $(P_{turb}/P)_{max}$ during the main sequence as a function of T_{eff} for $60M_\odot$ and $62M_\odot$ initial mass models with a mixing-length parameter of $\alpha = 0.5$.

models is the same at both temperatures and the differences in radius are small, these differences can be deemed as not significant.

Figure 4 shows the optical depth and density of the FeCZ at $T_{eff} = 40$kK and $T_{eff} = 25$kK respectively, as well as the HeCZ for the latter. Of note is the very similar behaviour in density and convective velocity, as well as the appearance of the HeCZ and FeCZ at the same optical depth for both the $60M_\odot$ model and the $62M_\odot$ model. Still there are clear differences: At $T_{eff} = 40$kK, the density of the $62M_\odot$ model is consistently lower, the density inversion in the FeCZ is stronger and the maximum convective velocity is higher.
As before, this is mainly due to the lower effective temperature of the $62M_\odot$ model. In Figure 5 the maximum convective velocities v_c^{max} at different temperatures for both $60M_\odot$ and $62M_\odot$ are shown, where it can be seen that the range around $T_{eff} = 40$kK is where v_c^{max} quickly ramps up (from around 4 km/s above 40kK to around 10 km/s at 35kK) as the convective motion in the FeCZ becomes much stronger during the main sequence evolution of the stellar models (see Grassitelli et al. 2015). This also explains the stronger density inversion of the $62M_\odot$ model.

Even so, as shown in Figures 5 and 6, v_c^{max} and the maximum turbulent pressure fraction $(P_{turb}/P)^{max}$ are continuously higher in the $62M_\odot$ model. This is consistent with Grassitelli et al., where it was shown that higher mass stars with correspondingly higher luminosities achieve higher maximum turbulent pressure fractions. Nonetheless, this effect is quite small, especially when compared to the significantly higher convective velocities and turbulent pressure fractions of models with different mixing-length parameters (see Sect. 3). Therefore the $62M_\odot$ model is still evaluated to be very similar to the $60M_\odot$ model. Substituting it for the $60M_\odot$ model in the following examinations allows comparing properties with luminosity values that are closer to those of models with other mixing-length parameters. This is useful because in observations the stellar mass can not be measured directly which means that comparing stellar models with luminosities as similar as possible is far more meaningful.

3.2 Envelope inflation

Inflation is the formation of extended stellar envelopes in massive stars during core hydrogen burning. It is associated with stars close to the Eddington limit and may be connected to sub-surface convection zones, as the process of envelope inflation decreases the opacity in the envelope (see Sanyal et al. 2015). We distinguish between the non-inflated core with core radius r_{core} and the inflated envelope, which contains very little mass. The core radius r_{core} is defined as the radius, where $\beta(r) = P_g/P < 0.15$ for the first time going from the core to the surface of the stellar model. To quantify inflation, the strength of inflation is defined as:

$$\frac{\Delta r}{r_{core}} := \frac{R_* - r_{core}}{r_{core}} \quad . \tag{11}$$

with R_* as the photospheric radius (definitions according to Sanyal et al. 2015).

Sanyal et al. (2015) suggests that stars above $40M_\odot$ show envelope inflation and density inversions during their main sequence evolution, which should also apply for the $60M_\odot$ (and $62M_\odot$) models examined here. Figures 7, 8 and 9 show the density profiles for the different mixing-length parameters at effective temperatures of 40kK, 25kK and 15kK respectively.

At $T_{eff} = 40$kK the HeCZ is not expected and the FeCZ does not have strong turbulent pressure and convective velocities yet (Grassitelli et al. 2015), which will be investigated further in Section 4.2. The density profile of the

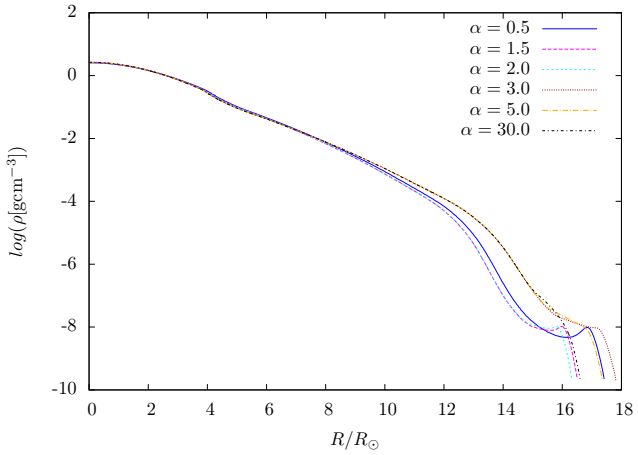

Figure 7: Density ρ as a function of stellar radius R for stellar models with $T_{\rm eff} = 40$kK and with different mixing-length parameters α. The models with $\alpha \geq 1.5$ have an initial mass of $60M_\odot$, while the model with $\alpha = 0.5$ has an initial mass of $62M_\odot$.

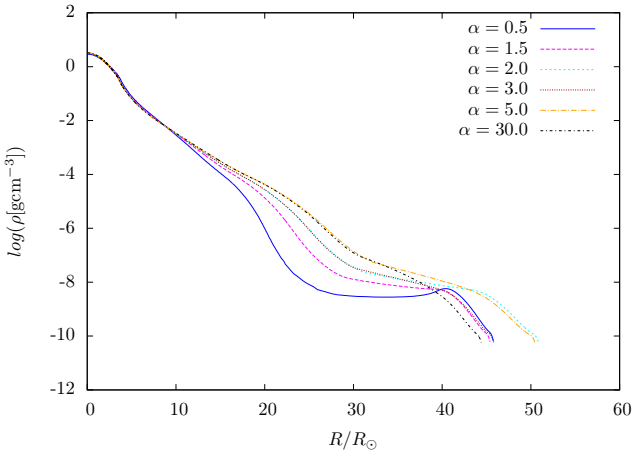

Figure 8: Density profiles for stellar models with $T_{\rm eff} = 25$kK and the same conditions for initial mass as in Fig. 7

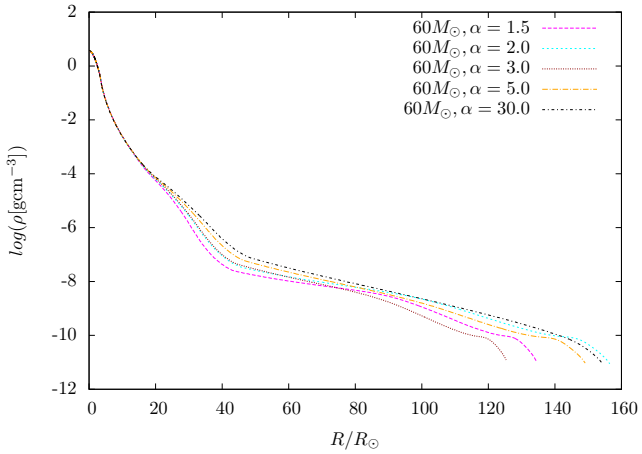

Figure 9: Density profiles for stellar models with $T_{\rm eff} = 15$kK. Shown are only models with initial mass $60M_\odot$ and mixing-length parameters $\alpha \geq 1.5$, as computation for the model with $\alpha = 0.5$ stopped before it reached $T_{\rm eff} = 15$kK.

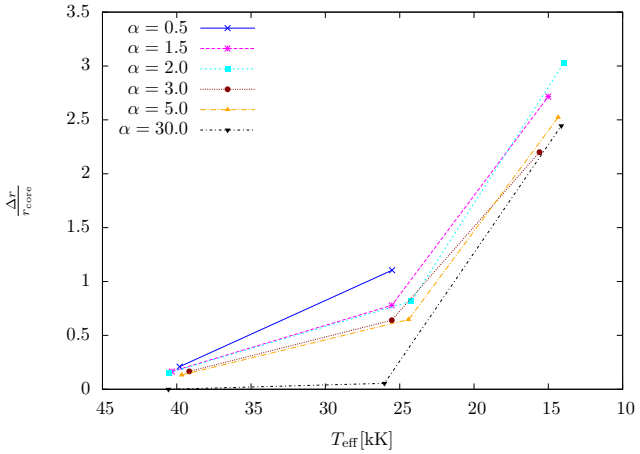

Figure 10: Strength of inflation, defined in Eq. 11, as a function of effective temperature. Shown as dots are stellar models with $T_{\rm eff} = 40$kK, $T_{\rm eff} = 25$kK and $T_{\rm eff} = 15$kK and with different mixing-length parameters α. The models with $\alpha = 0.5$ have an initial mass of $62M_\odot$, while the models with other α have an initial mass of $60M_\odot$. The model for $T_{\rm eff} = 15$kK with $\alpha = 0.5$ could not be computed. Lines are only used as an indication which models have the same mixing-length parameter.

model with $\alpha = 0.5$ shows a clear density inversion, as do those with $\alpha = 1.5$ and $\alpha = 2.0$. In these models, the convective motions are weaker than in the models of larger mixing-length parameters. Therefore stronger density inversions and inflation are expected, as a larger decrease in opacity is needed to transport energy outwards. The expectation is confirmed in the profiles of $T_{\rm eff} = 25$kK and $T_{\rm eff} = 15$kK, although density inversions for $\alpha = 1.5$ and $\alpha = 2.0$ disappear, inflation increases nonetheless. To quantify the inflation in our examined models, Table 2 shows the effective temperature, stellar radius R_*, core radius $r_{\rm core}$ and the strength of inflation $\Delta r/r_{\rm core}$.

At $T_{\rm eff} = 40$kK (Fig. 7), the strength of inflation is very small, for $\alpha = 30$ there is no inflation at all. During main sequence evolution the strength of inflation increases, which is expected since the FeCZ, which might drive inflation (Sanyal et al.), becomes much stronger during the time on the main sequence. At $T_{\rm eff} = 15$kK (Figure 9), the models of all mixing-length parameters show clearly inflated envelopes ($\Delta r/r_{\rm core} \geq 2$), even for $\alpha = 30$.

Generally it is shown that models with small mixing-length parameters produce stronger inflation than models where the parameter is large. At both 40kK and 25kK, $\alpha = 0.5$ shows the highest strength of inflation and the inflated envelope can be very clearly seen in Figures 7 and 8. The strength of inflation is also illustrated in Figure 10. The amount of data points examined here is too low for a definitive assessment of inflation. The values shown seem to contradict the idea of a clear correlation between the mixing-length parameter and the strength of inflation at first,

Table 2: Properties of the stellar models which are nearest in effective temperature to $T_{\rm eff}$ = 40kK, $T_{\rm eff}$ = 25kK and $T_{\rm eff}$ = 15kK, including mixing-length parameter α, $T_{\rm eff}$, stellar radius R_*, core radius $r_{\rm core}$ and strength of inflation $\Delta r/r_{\rm core}$. The models with $\alpha = 0.5$ have an initial mass of $62 M_\odot$, the models with other mixing-length parameters have an initial mass of $60 M_\odot$. The core radius $r_{\rm core}$ is defined as the radius within the star, where $\beta(r) = P_{\rm g}/P < 0.15$ for the first time. Strength of inflation $\Delta r/r_{\rm core}$ is calculated with Eq. 11 and expected to be unambiguous for $\Delta r/r_{\rm core} \geq 2$ (Sanyal et al. 2015).

	α	$T_{\rm eff}$[K]	$R_*[cm]$	$r_{\rm core}[cm]$	$\frac{\Delta r}{r_{\rm core}}$
40kK	0.5	39805	1.22E+012	1.01E+012	0.210
	1.5	40324	1.15E+012	9.92E+011	0.165
	2	40552	1.14E+012	9.91E+011	0.152
	3	39157	1.25E+012	1.07E+012	0.166
	5	39672	1.21E+012	1.07E+012	0.132
	30	40562	1.16E+012	1.16E+012	0.000
25kK	0.5	25513	3.20E+012	1.52E+012	1.105
	1.5	25541	3.18E+012	1.79E+012	0.778
	2	24212	3.56E+012	1.96E+012	0.817
	3	25535	3.21E+012	1.95E+012	0.641
	5	24402	3.54E+012	2.15E+012	0.647
	30	26027	3.11E+012	2.94E+012	0.055
15 kK	1.5	15006	9.41E+012	2.53E+012	2.716
	2	13946	1.10E+013	2.72E+012	3.032
	3	15590	8.78E+012	2.74E+012	2.200
	5	14336	1.04E+013	2.96E+012	2.523
	30	14124	1.08E+013	3.14E+012	2.445

since some models with a larger mixing-length parameter have higher strengths of inflation than those with a smaller mixing-length parameter.

This is more likely explained by differences in the actual effective temperature and the correlation being small rather than a fundamental misunderstanding of inflation. Particularly for the mixing-length parameters $\alpha = 1.5, 2.0, 3.0, 5.0$, the differences in inflation seem to be small. Therefore a slightly lower effective temperature can already increase the inflation of a model with a larger mixing-length parameter above that of a model with a smaller parameter. Big differences in the strength of inflation can only be seen when the mixing-length parameter is very different as well. The strength of inflation for models with $\alpha = 30$ is always less than that of $\alpha = 0.5$, $\alpha = 1.5$ and $\alpha = 2$ and models with $\alpha = 0.5$ are always inflated to a stronger degree than any other model with the same temperature.

4 Properties of sub-surface convection zones and their connection to macroturbulence

4.1 The behaviour of maximum convective velocities and turbulent pressure fraction

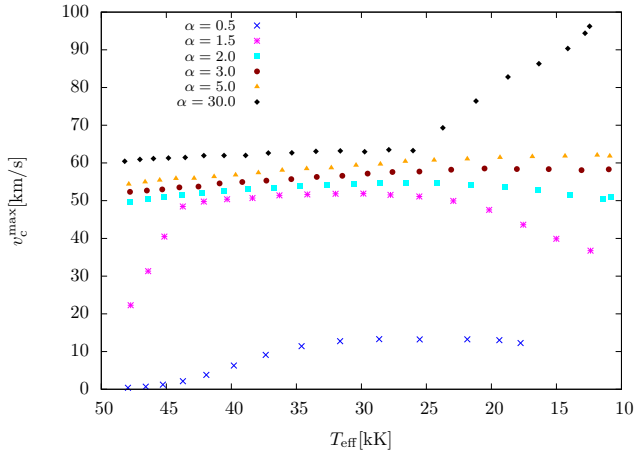

Figure 11: Behaviour of the maximum convective velocity v_c^{max} as a function of effective temperature in stellar models with different mixing-length parameters, where we limit v_c with Eq. 10. The model with $\alpha = 0.5$ has an initial mass of $62M_\odot$, the models with higher mixing-length parameters have an initial mass of $60M_\odot$.

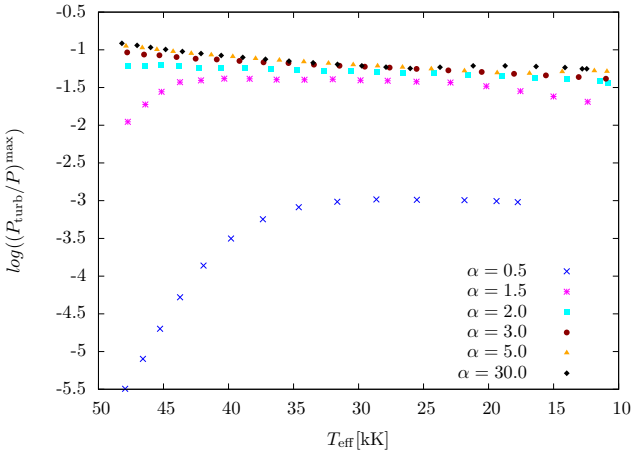

Figure 12: Behaviour of the maximum turbulent pressure fraction $(P_{turb}/P)^{max}$ calculated with Eq. 5 in stellar models with different mixing-length parameters as a function of T_{eff}. A non-logarithmic scale is shown in Fig. 21.

Following the previous results the properties of the convective regions for the different mixing-length parameters are examined further. Figure 11 shows the maximum convective velocity v_c^{max} for each model, limited to the local isothermal sound speed $c_{s,iso}$.

The maximum convective velocities for all mixing-length parameters except for $\alpha = 0.5$ are so high that they reach $c_{s,iso}$ during their evolution, which can be seen in Figure 20. For $\alpha = 1.5$, above $T_{eff} \approx 45$kK and below $T_{eff} \approx 20$kK the maximum convective velocities do not approach the local sound speed. Below $T_{eff} \approx 15$kK the maximum convective velocity is lower than the local sound speed for $\alpha = 2$ as well. For the examined mixing-length parameters of $\alpha \geq 3.0$ the v_c^{max} always reaches the limitation $v_c^{max} = c_{s,iso}$. The maximum convective velocities for models with mixing-length parameters of $\alpha = 0.5$ and $\alpha = 1.5$ follow the expectation of increasing in the early main sequence as convective motions in the FeCZ become stronger and decreasing in the late main sequence, as the FeCZ moves deeper into the envelope (see Grassitelli et al. 2015). For models with $\alpha = 2$ this is the case as well but the effect is less pronounced, as the sound speed is reached for most of the main sequence.

Apparently, the local sound speed at the point of the maximum convective velocity is different for each mixing-length parameter. This might be explained by the formula for $c_{s,iso}$ (Eq. 4). The local sound speed depends on both the local temperature and the local mean molecular weight. While the iron opacity bump always occurs at $log(T) \approx 5.3$, the maximum convective velocity can be reached at different points in the FeCZ (the convective velocities for the HeCZ should be much lower, see Sect. 4.2). For larger mixing-length parameters the FeCZ extends deeper into the interior of the star and thus contains higher local temperatures than models with smaller mixing-length parameters due to convective overshooting. The highest local sound speed of the convection zone is reached at the highest local temperature, therefore larger mixing-length parameters show higher maximum convective velocities, even when limited to the isothermal sound speed.

The maximum convective velocity where it reaches the sound speed remains relatively constant during the main sequence evolution, since the temperature where the iron opacity bump occurs is fixed. The maximum convective velocity (therefore the local isothermal sound speed) increases slightly due to the FeCZ becoming more extended during the evolution. The exception for this trend are the models with $\alpha = 30$ beginning below $T_{eff} \approx 25$kK. There a strong and steady increase in v_c^{max} can be seen (which is not present in the non-physical unlimited maximum convective velocities in Figure 20). The effect is caused by the second iron opacity peak deeper in the star, which becomes relevant at this temperature. Normally, the convective velocities of the second iron opacity should be much smaller than those of the outer iron opacity peak, as is the case for all other mixing-length parameters. In the case of $\alpha = 30$, the convective velocities become very high. Since the second iron opacity peak is located at significantly higher temperatures, the limiting local sound speed is much higher as well and as a result a higher convective velocity is reached in the second FeCZ. This effect is shown in Figure 22 for $T_{eff} = 15$kK. Nonetheless, even with this effect, only the outer iron opacity peak is investigated, since the second peak is expected to be too deep in the star to cause

macro- or microturbulence. Figure 22 also shows that the HeCZ might become important for models with $\alpha = 30$, which will be investigated in Section 4.2.

Generally, as would be the case with unlimited (transonic) convective velocities (Figure 20), a larger mixing-length parameter correlates to higher convective velocities. These results agree with the MLT, where a larger mixing-length parameter means a larger length l over which a gas blob can be accelerated before it dissolves. As a consequence higher convective velocities are reached (see Eq. 3).

Also of interest is the maximum turbulent pressure fraction $(P_{\rm turb}/P)^{\rm max}$ of the investigated models, which is shown in Figure 12. The total pressure P consists only of the gas and radiation pressure: $P = P_{\rm g} + P_{\rm r}$. The logarithmic scale is chosen due to the large differences in the turbulent pressure between the models with $\alpha = 0.5$ and $\alpha = 30$, a non-logarithmic scale is used in Fig. 21. Results from Grassitelli et al. (2015) indicate that the maximum turbulent pressure fraction increases during the main sequence evolution as the inflation becomes stronger, reaching a maximum in the O supergiant regime, then decreasing again in the B supergiant regime as the FeCZ moves deeper into the stellar envelope. The models that were computed with $\alpha = 0.5$ and $\alpha = 1.5$ generally follow this expectation, although $\alpha = 0.5$ could not be evolved far enough to see a significant drop in the turbulent pressure fraction.

For models with mixing-length parameters of $\alpha = 2$ and larger, this is not the case. Instead, the maximum turbulent pressure fraction is highest during the beginning of the main sequence evolution, decreasing with lower effective temperatures. This behaviour is strongest for $\alpha = 30$ and $\alpha = 5$, which have the highest turbulent pressure fractions (see also Figure 21, where $(P_{\rm turb}/P)^{\rm max}$ is shown non-logarithmically). This effect is explained due to Eq. 5, $v_{\rm c}^{\rm max}$ for these large mixing-length parameters remains almost constant during the main sequence evolution due to its sound speed limitation, as discussed. On the other hand, the density of the envelope where the FeCZ is located decreases during main sequence evolution as seen in Figures 7 - 9. The turbulent pressure fraction is calculated a posteriori with Eq. 5, causing a decreasing maximum turbulent pressure fraction. This effect will be examined further in Sect. 4.2 when looking at the optical depth of the convection zones as well as their density.

Models with larger mixing-length parameters have higher maximum turbulent pressure fractions and correspondingly higher maximum convective velocities, as is to be expected according to Eq. 5. The increase of $(P_{\rm turb}/P)^{\rm max}$ for models with $\alpha = 30$ below $T_{\rm eff} \approx 25$kK will be investigated in the next section as well.

For models with a mixing-length parameter of $\alpha = 3$ and above the maximum convective velocity is equivalent to the maximum local sound speed of the convection zone at all times in their main sequence evolution and will be referred to as 'large mixing-length parameters'. Models with $\alpha = 2$ and below do not always reach the isothermal sound speed and will be referred to as 'small mixing-length parameters'. To bear in mind is that $\alpha = 2$ seems to be a borderline case, as the maximum convective velocities do reach the sound speed for a large part of the main sequence evolution, but not at all times. Nonetheless it will be categorised as 'small', especially since a value of $\alpha = 2$ is still covered by calibrations of the mixing-length parameter for the Sun (Pols 2009).

4.2 Properties of the convective zones as a function of optical depth

Following the results from Section 4.1, the structure of the outer layers of the models at $T_{\rm eff} = 40$kK, $T_{\rm eff} = 25$kK and $T_{\rm eff} = 15$kK is investigated further. This is done for density ρ, temperature T and pressure P as a function of optical depth τ, with coloured indications of the convection zones for convective velocities $v_{\rm c}$ and turbulent pressure fractions $P_{\rm turb}/P$. To better distinguish the models with different mixing-length parameters α, the aforementioned plots were redone with offsets in their respective y-values. All plots can be found in Figures 23 - 40 in Sect. 7.1.1.

4.2.1 The convective zones

The models of all mixing-length parameters show the same convection zones, associated with the partial ionisation of helium at $log(T) \approx 4.5$ and iron at $log(T) \approx 5.3$ as seen in Fig. 25, 26, 31, 32, 37 and 38. The HeCZ does not exist at $T_{\rm eff} = 40$kK, but is present for both $T_{\rm eff} = 25$kK and $T_{\rm eff} = 15$kK. Its upper boundary moves from an optical depth of $log(\tau) \approx 0.1$ at $T_{\rm eff} = 25$kK close to the surface deeper into the envelope to $log(\tau) \approx 0.8$ at $T_{\rm eff} = 15$kK, which agrees with the results in Grassitelli et al. (2015). Its radial extent only increases from $\Delta log(\tau) \approx 0.8$ at $T_{\rm eff} = 25$kK to $\Delta log(\tau) \approx 1.0$ at $T_{\rm eff} = 15$kK with similar values for all mixing-length parameters except $\alpha = 5$ and $\alpha = 30$. The HeCZ for $\alpha = 30$ at $T_{\rm eff} = 15$kK has a radial extent of $\Delta log(\tau) \approx 2.0$, which is so high that its lower boundary almost reaches the upper boundary of the FeCZ.

The extent of the HeCZ corresponds to it becoming important for models with $\alpha = 30$ late in the main sequence evolution. The convective velocities are almost as high as in the FeCZ. Since they are limited by the local isothermal sound speed as well and the temperatures in the HeCZ are lower, they do not reach values as high (see eg. Fig. 37). The turbulent pressure fraction however reaches even higher values in the HeCZ than the FeCZ, by $\sim 1\%$. This is explained by the behaviour of the pressure P in the convection zones. While the turbulent pressure is lower in the HeCZ due to both lower convective velocities and density (see Fig. 35), the turbulent pressure fraction $P_{\rm turb}/P$ is still larger because the total pressure is smaller in the HeCZ (see Fig. 40). For the HeCZ, $P_{\rm turb}/P$ is highest at $log(P) \approx 2.9$ while it is highest at $log(P) \approx 5.1$ in the FeCZ. For $\alpha = 5$, the HeCZ at $T_{\rm eff} = 15kK$ is slightly more

extended than the HeCZs for smaller mixing-length parameters as the turbulent pressure fraction exceeds that of the FeCZ by $\sim 0.5\%$. If the mixing-length parameter is large enough enough, even the HeCZ becomes important, despite the opacity bump being far smaller (see Cantiello et al. 2009). It is difficult to determine whether this might be a realistic result or rather regarded as an artefact of the stellar code due to limitation of v_c.

The FeCZ exists at all times of the main sequence evolution in the $60 M_\odot$ models. Its upper boundary is at a similar optical depth for all mixing-length parameters, which moves deeper into the envelope during evolution, from $log(\tau) \approx 1.6$ at $T_{\rm eff} = 40$kK to $log(\tau) \approx 2.2$ at $T_{\rm eff} = 40$kK and $log(\tau) \approx 2.9$ at $T_{\rm eff} = 15$kK. This corresponds to results from Grassitelli et al. (2015). Slight differences in the effective temperatures of the models with different mixing-length parameters are presumably responsible for variations in the optical depths of the upper boundaries for both HeCZ and FeCZ.

The lower boundary of the FeCZ however is clearly dependent on the mixing-length parameter α, as can be seen in Figures 23 through 40. At all three examined effective temperatures the FeCZ reaches deeper into the envelope the larger α is. The higher convective velocities in models with larger mixing-length parameters cause significant convective overshooting beyond the iron opacity peak at $log(T) \approx 5.3$. The FeCZ also becomes more extended from $T_{\rm eff} = 40$kK to $T_{\rm eff} = 25$kK for all mixing-length parameters. The effect is stronger for small mixing-length parameters and there is almost no increase in the extent of the FeCZ for $\alpha = 30$. From $T_{\rm eff} = 25$kK to $T_{\rm eff} = 15$kK, there is no clear further increase in the extent of the FeCZ for any of the remaining mixing-length parameters. As the turbulent pressure is not included in our stellar model computation, it can not increase the extent of the FeCZ, as was the case in Grassitelli et al. (2015). Here only inflation increases it, which is stronger for smaller mixing-length parameters. It also counteracts the decreasing turbulent pressure fraction in models with large mixing-length parameters, as density decreases less steeply outwards in an inflated envelope. During the late part of the main sequence evolution inflation does not seem to be enough to further increase the extent of the FeCZ, even though inflation is considerably stronger at $T_{\rm eff} = 15$kK than at $T_{\rm eff} = 25$kK.

One possible explanation is that the HeCZ instead of the FeCZ is actually responsible for a significant part of the inflation at $T_{\rm eff} = 15$kK. Looking at Figures 35 and 36, this is confirmed by the visible decrease in slope for density in the HeCZ, except for $\alpha = 30$ where the effect is less significant. The inflation in the FeCZ actually seems to decrease compared to models with $T_{\rm eff} = 25$kK, especially for larger mixing-length parameters. The results confirm that large convective velocities due to high turbulent pressure fractions inhibit inflation, as more energy can be transported upwards (see Sanyal et al. 2015).

4.2.2 The behaviour of convective velocities in the CZs

Overall, the convective velocities throughout the FeCZ as well as the HeCZ are higher for larger mixing-length parameters. The behaviour of v_c for small mixing-length parameters meets the expectation of reaching its highest values roughly in the middle of the convection zones for all examined effective temperatures, as can be seen for example in Figures 25, 31, 37. According to the MLT, the blobs of gas are accelerated upwards or downwards in a convection zone and decelerated at either end. For large mixing-length parameters, where the convective velocity reaches the isothermal sound speed almost everywhere in the FeCZ, the maximum convective velocity is instead reached at the lower boundary of the convection zones. There temperature, and therefore local isothermal sound speed are highest. This result is non-realistic, as a significant amount of additional overshooting should occur, where the gas blobs are decelerated.

The highest values for v_c in the FeCZ correspond to the maximum convective values discussed in Section 4.1 for all mixing-length parameters and effective temperatures shown. The notable exception is the model with $\alpha = 30$ at $T_{\rm eff} = 15$kK, where the maximum convective velocity is reached in the CZ of the second iron opacity peak instead.

The results again show the mixing-length parameter of $\alpha = 2$ as a transitional value, above which the properties of the results are significantly altered due to v_c reaching the sound speed throughout most or all (in the models with $\alpha = 30$) of the FeCZ.

4.2.3 The behaviour of the turbulent pressure fraction in the CZs

In most cases, the turbulent pressure fraction is highest in the FeCZ and increases with the mixing-length parameter throughout the convection zones, although there are a few exceptions for the maximum turbulent pressure fraction as shown in Sect. 4.1.

For small mixing-length parameters ($\alpha \leq 2$) the behaviour of the turbulent pressure fraction can be seen for example in Figures 28, 34 and 40, corresponds to that of the convective velocities, as it reaches its highest values approximately in the middle of the convection zones. The models with $\alpha = 0.5$ specifically have very small turbulent pressure fractions in the HeCZ as well as the FeCZ. They are less than 1%, even at $T_{\rm eff} = 25$kK, where the effect of turbulent pressure is the most significant.

For the models with $\alpha = 3$ and $\alpha = 5$, the behaviour of the turbulent pressure inside the FeCZ changes. The distance of the highest turbulent pressure fraction from the upper boundary of the convection zone decreases during the main sequence evolution. At the same time, the maximum turbulent pressure fractions decrease as well. The move

towards the upper boundary of the convection zone happens even though both the density and the convective velocity, due to limitation to the local isothermal sound speed, are always lowest at this boundary (see Eq. 5). The cause is found in the behaviour of pressure P throughout the convective zones, see eg. Figures 28, 34 and 40. As the effective temperature decreases during main sequence evolution, the difference between the pressure of the upper and the lower boundaries (where v_c^{max} is located for large mixing-length parameters) increases strongly. Taking the models with $\alpha = 3$ as an example, the pressure difference is $\Delta log(P) \approx 1.4$ at $T_{\rm eff} = 40$kK, increasing to $\Delta log(P) \approx 1.8$ at $T_{\rm eff} = 25$kK and reaching $\Delta log(P) \approx 2.1$ at $T_{\rm eff} = 15$kK. This is caused both by an increase in the radial extent of the FeCZ and by the increase in pressure inwards becoming steeper for later models, especially at $T_{\rm eff} = 15$kK, where the FeCZ is not more extensive than at $T_{\rm eff} = 25$kK. This effect is stronger for $\alpha = 5$ and $\alpha = 30$. The model with $\alpha = 30$ even has its highest turbulent pressure fraction directly at the upper boundary of its convection zones for all three temperatures.

4.2.4 Influence of convection on the temperature

The convection zones have a clear effect on the local temperature as well, see e.g. Fig. 25, 31 and 37. In the FeCZ there is a visible bump where the temperature decreases less steeply outwards. This effect is stronger the larger the mixing-length parameter is, meaning with higher convective velocities. For the model with $\alpha = 30$ and $T_{\rm eff} = 15$kK, a bump becomes visible in the HeCZ as well. Here the cause for the change in effective temperature for models with different mixing-length parameters at the same luminosity discussed in Section 3 can be seen. Models with the same effective temperature as used here have a cooler interior the larger α is as more of the heat is transported towards the surface when gas blobs travel with higher velocities and a longer distance before dissolving. The change of local temperatures in the convection zones supports this explanation.

Looking at the local temperature reveals the extension of the convection zones around the iron and helium opacity bumps as well. The helium opacity bump occurs at $log(T) \approx 4.6$ which is the lower boundary of the HeCZ in all models except for $\alpha = 30$ and $T_{\rm eff} = 15$kK, where the convection zone is much more extensive. The upper boundary is located at a similar temperature of $log(T) \approx 4.45$ for all models at $T_{\rm eff} = 25$kK and as the effective temperature decreases to $T_{\rm eff} = 15$kK it moves to $log(T) \approx 4.35$. The upper boundary of the FeCZ starts at similar local temperatures for all mixing-length parameters as well, moving from $log(T) \approx 4.97$ at $T_{\rm eff} = 40$kK to $log(T) \approx 4.90$ at $T_{\rm eff} = 15$kK. The lower boundary of the FeCZ on the other hand is strongly influenced by the mixing-length parameter. The iron opacity bump is located at $log(T) \approx 5.3$. For the models with $\alpha = 0.5$, this is also the lower boundary, while the FeCZ extends deeper into the envelope the larger α is. This shows that significant convective velocities cause strong overshooting deeper into the star, as is the case for the HeCZ in the $\alpha = 30$ model at $T_{\rm eff} = 15$kK as well. The result corresponds to the finding that v_c is highest at the lower boundary of the convection zone for large mixing-length parameters.

4.2.5 Influence of convection on the density

The influence of convection zones on density in the stellar envelope is also shown, eg. in Figures 23, 29 and 35. As expected (see Sanyal et al. 2015), larger mixing-length parameters imply a stronger decrease in density outwards, as inflation is suppressed by stronger turbulent motions. For models with $\alpha = 0.5$, there are clear density inversions at both $T_{\rm eff} = 40$kK and $T_{\rm eff} = 25$kK with similar strength of inversion. Density inversions are also present at $T_{\rm eff} = 40$kK for $\alpha = 1.5$ and $\alpha = 2$, which are becoming weaker for larger mixing-length parameters. These density inversions have disappeared when the models reach $T_{\rm eff} = 25$kK, even though inflation becomes stronger (see Section 3.2). For models with $\alpha \geq 3$, density inversions disappear completely, although there are still decreases in the slope of the density present, which are shallower the smaller the mixing-length parameter is. This shows that for large mixing length parameters with high enough convective velocities, the convective flux is high enough to completely prevent density inversions. This confirms the results from Sanyal et al. (2015) that models with density inversions are always inflated, but density inversions are not needed for inflation.

The upper boundaries of the HeCZ and the FeCZ move deeper into the envelope during main sequence evolution, meaning higher optical depth of the convective zones. Still, the boundaries have lower densities for lower effective temperatures. This is due to expansion and mass loss of the stellar models, which cause the density of the envelope to decrease over the course of the main sequence. As the density on the surface of models with a similar effective temperature is approximately the same, the models with smaller mixing-length parameters show higher densities below the FeCZ, which is the source of the strongest density changes for most models, with stronger changes for smaller mixing-length parameters.

For small mixing-length parameters, the inflection point of density, or for models with a density inversion the density minimum, in the FeCZ corresponds to the highest convective velocities and turbulent pressure fractions. For large mixing-length parameters this is not the case, as discussed for the behaviour of v_c and $P_{\rm turb}/P$. Looking at Equation 3, the density inflection point or the density minimum apparently is the point in the convection zone where the superadiabaticity $\nabla - \nabla_{\rm ad}$ is highest.

4.2.6 Influence of convection on the pressure

The effect the convection zones have on the local pressure P is similar to the effect on temperature T, as seen for example in Figures 28, 34 and 40. There are bumps in the outward decrease of pressure, which are stronger for larger mixing-length parameters. Pressure is defined as (Pols 2009)

$$P = P_{\rm g} + P_{\rm r} = \frac{1}{3}aT^4 + \frac{\mathcal{R}}{\mu}\rho T \tag{12}$$

where a is the radiation constant and $\mathcal{R}$ is the universal gas constant. This shows that pressure is more strongly dependent on temperature than density, therefore the pressure profiles for different mixing-length parameters follow those of the local temperature and the same bumps are created. The total pressure in the convection zone influences the turbulent pressure fraction as well. This does not seem to influence the position of $(P_{\rm turb}/P)^{\rm max}$ in the models however, since the changes in P are only significant for large mixing-length parameters in the FeCZ, where the maximum turbulent pressure fraction is always located at the upper boundary of the convection zone.

4.3 Comparison with observations regarding macroturbulence

In Grassitelli et al. (2015), a connection between the relative strength of the turbulent pressure in sub-surface convection zones and the strength of macroturbulence on the surface was found. In order to investigate how the mixing-length parameter influences the correlation, the derived values for surface temperature ($T_{\rm eff}$), gravity ($log(g)$) and macroturbulent velocity ($v_{\rm macro}$) from a spectroscopic analysis of ~ 300 Galactic OB stars in Simón-Díaz (2015) are used. Figure 13 shows a spectroscopic HRD (sHR, see Langer & Kudritzki 2014) of the computed stellar tracks as well as the observed OB stars. Since only a few stars lie on the stellar tracks, a wider range of stars is used for comparison, as indicated in the sHR. Figure 14 shows the macroturbulent velocities of the OB stars as a function of the maximum turbulent pressure fraction. The maximum turbulent pressure fraction of the stars was fitted from the values of the models with $\alpha = 1.5$ according to their effective temperature. Due to the low amount of observational data, the correlation is not as clear as in Grassitelli et al. (2015), particularly since only four stars fall in the range used between $T_{\rm eff} = 25$kK and $T_{\rm eff} = 15$kK. Nonetheless it can be said that there is a possible linear correlation similar to the one shown in Grassitelli et al. (2015).

Because there is not enough data to assess the existence of a correlation between the turbulent pressure fraction and macroturbulent velocities for models with different mixing-length parameters, we only investigate the different trends shown in Sect. 4.1. Figures 15 - 17 show the same process as Fig. 14, but with stars fitted to the tracks of models with $\alpha = 0.5$, $\alpha = 2$ and $\alpha = 30$ respectively.

For the models with $\alpha = 0.5$ and $\alpha = 30$, there is clearly no correlation. Even with this small data set, these values can therefore be ruled out as useful calibrations for the mixing-length parameter, barring contradictory future observational data and assuming that the turbulent pressure is indeed responsible for macroturbulence. For the models with $\alpha = 2$, the case is not as clear. While there is still a possible correlation between the maximum turbulent pressure fraction and macroturbulent velocities, it does not seem to be as good as the calibration with $\alpha = 1.5$. The small amount of data for the luminosity range combined with uncertainties in the measurements preclude a definite conclusion however.

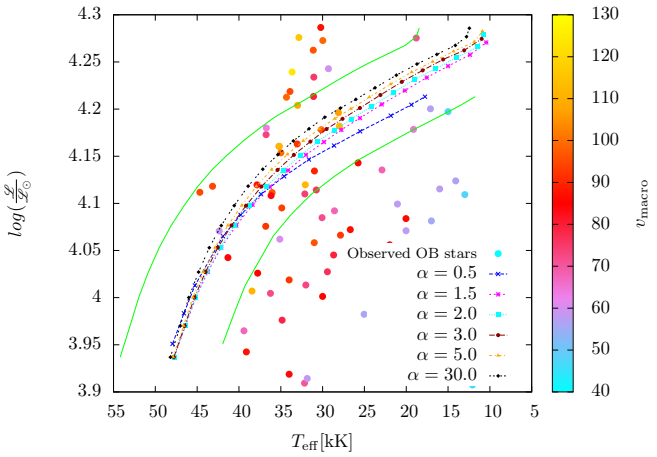

Figure 13: Spectroscopic HRD (Langer & Kudritzki 2014) of the computed stellar tracks. Circles represent observed OB stars, colour coded according to the macroturbulent velocity $v_{\rm macro}$ (Simón-Díaz 2015).The green lines represent a range close to the stellar tracks (distance of $\Delta T_{\rm eff} = 6$kK from the tracks with $\alpha = 0.5$ and $\alpha = 30$ for the respective values of $log(\mathscr{L}/\mathscr{L}_\odot)$) , observed stars from this range are used for comparison of the turbulent pressure fraction and macroturbulent velocity.

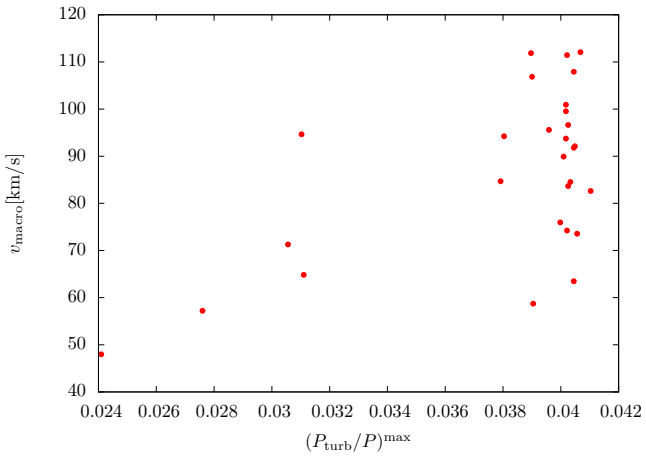

Figure 14: Macroturbulent velocity of observed OB stars near the stellar evolution tracks, according to Fig. 13, as a function of the maximum turbulent pressure fraction. The maximum turbulent pressure fraction for the stars was derived from a fitting of the track described in Sect. 4.1 for models with $\alpha = 1.5$.

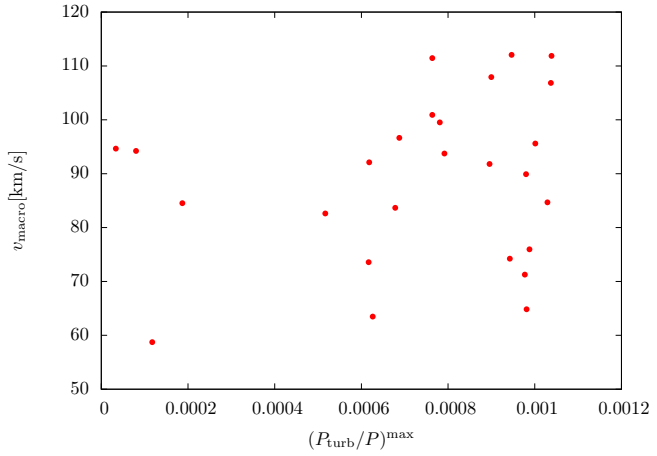

Figure 15: Same as Fig. 14, but from fitting the stars to the track of models with $\alpha = 0.5$.

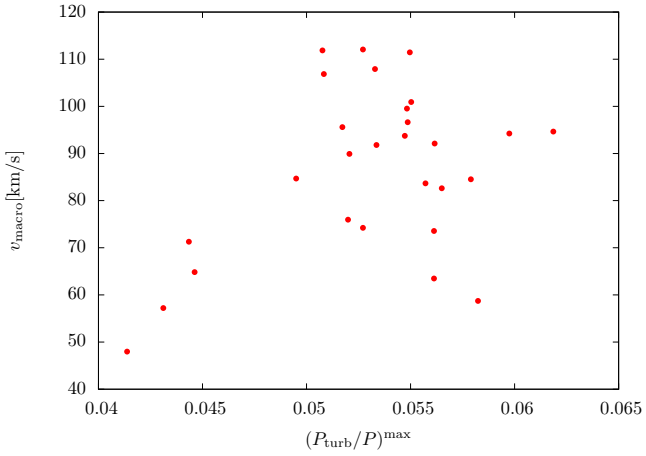

Figure 16: Same as Fig. 14, but from fitting the stars to the track of models with $\alpha = 2$.

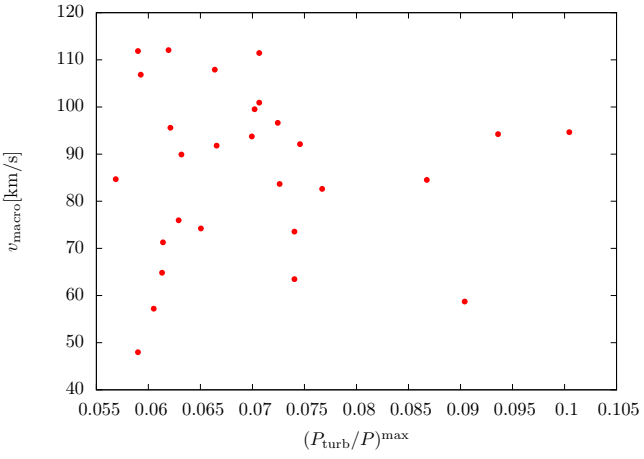

Figure 17: Same as Fig. 14, but from fitting the stars to the track of models with $\alpha = 30$.

5 Microturbulence

5.1 Results

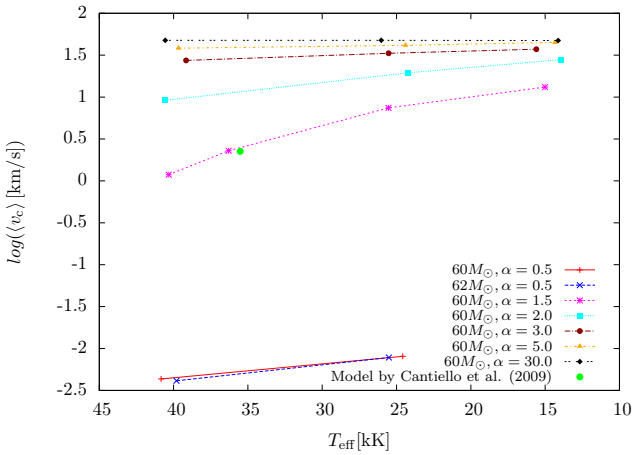

Figure 18: Average convective velocity $\langle v_c \rangle$ in the FeCZ on a logarithmic scale as a function of effective temperature $T_{\rm eff}$ for models with $60M_\odot$ initial mass and different mixing-length parameters α, as well as a model with an initial mass of $62M_\odot$ and $\alpha = 0.5$. The dots indicate the models for which $\langle v_c \rangle$ was calculated. The lines are only intended to indicate models with the same initial mass and mixing-length parameter. Additionally, the average convective velocity of the $60M_\odot, \alpha = 1.5$ model presented in Cantiello et al. (2009) is shown as a comparison.

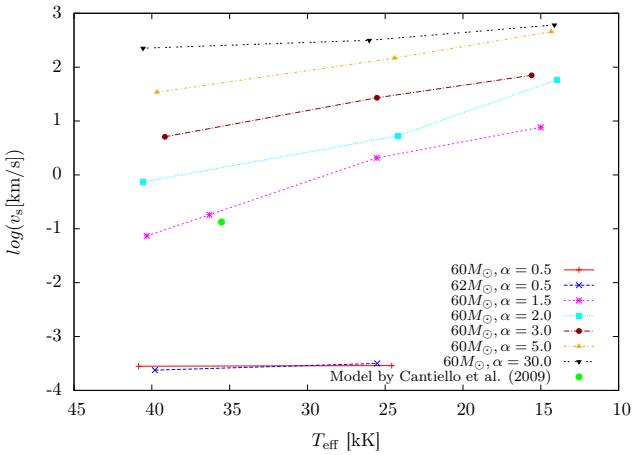

Figure 19: Upper limits for the surface velocity v_s, calculated using Eq. 7, as a function of $T_{\rm eff}$ for the same models shown in Fig. 18. The dots indicate for which models an upper limit for v_s was calculated. The lines are only intended to indicate models with the same initial mass and mixing-length parameter. The value $\langle v_c \rangle \cdot \sqrt{M_c \frac{\rho_c}{\rho_s}}$ for the model presented in Cantiello et al. (2009) was calculated from properties of the stellar model given therein.

The previous results have shown that the FeCZ influences properties in the stellar envelopes much more than the HeCZ in most computed models. Thus only the FeCZ is expected to be relevant in causing microturbulence (Cantiello et al. 2009). For the model with $\alpha = 30$ and $T_{\rm eff} = 15$kK however, convective velocities are almost as high in the HeCZ as in the FeCZ. Therefore this model will be examined as well. Since the comparison for the $60M_\odot$ and the $62M_\odot$ models at a mixing-length parameter of $\alpha = 0.5$ was only made regarding macroturbulence, both models will be considered here.

Following the method of Cantiello et al., the average convective velocity was calculated, which is defined according to Equation 6. The pressure scale height H_P was calculated as in Equation 2. For large mixing-length parameters α the mixing length $\alpha H_{\rm P}$ becomes very large, for $\alpha = 30$ it is greater than the extent of the FeCZ. In those models, the range over which the convective velocity is averaged is instead limited to the extent of the convective zone. As before models with three effective temperatures, $T_{\rm eff} = 40, 25, 15$kK are examined. Additionally, the calculations are done for a model with $\alpha = 1.5$ at $t = 2.38 \times 10^6$yrs as a direct comparison with Cantiello et al. (2009). From the average convective velocity, an upper limit to the surface velocities of the stellar models can be calculated according to Equation 7. The upper boundary of the convection zone R_c, as well as the results for the local pressure scale height $H_{\rm P}$, the average convective velocity $\langle v_c \rangle$, the isothermal Mach number M_c (Eq. 8) at radius R_c and the resulting upper limit for v_s are listed in Table 4.

From $T_{\rm eff} = 40$kK to $T_{\rm eff} = 15$kK, the pressure scale height $H_{\rm P}$ grows by two orders of magnitude. Looking at Equation 2, this happens due to an increasing radius R_c, correlated to inflation (see Sect. 3.2) combined with a decreasing density ρ_c at the upper boundary of the FeCZ as demonstrated in Sect. 4.2. The stellar mass also decreases over time due to mass loss. This happens because the upper boundary of the FeCZ moves deeper into the envelope with decreasing surface temperature. On the other hand, it is similar for models of all mixing-length parameters at a given temperature, corroborating the finding that the FeCZ does not significantly influence stellar structure (Grassitelli et al. 2015).

The average convective velocities near the upper boundary of the FeCZ, shown in Figure 18, increase with decreasing surface temperatures for the models with all considered mixing-length parameters except $\alpha = 30$. This is caused by the increased pressure scale height, since the convective velocities become larger deeper into the FeCZ. This result agrees with Cantiello et al. (2009). For models with $\alpha = 30$ the convective velocities are averaged over the entire FeCZ at all considered temperatures, therefore the average convective velocities differ by less than 0.7% as the v_c in the FeCZ does not change significantly for $\alpha = 30$, which was determined in Sections 4.1 and 4.2. At a fixed surface temperature, the average convective velocities increase with a larger mixing-length parameter, which agrees with the results from previous sections.

The average convective velocities for the models with $\alpha = 0.5$ are approximately the same for $60M_\odot$ and $62M_\odot$.

The differences between the models are smaller than the numerical uncertainties introduced through determining R_c and H_P. The differences in effective temperatures cause another uncertainty. The average convective velocity is very small for both $T_{eff} = 40$kK and $T_{eff} = 25$kK with values of $\sim 4 \times 10^{-3} - 8 \times 10^{-3}$km/s.

In the models with $\alpha = 1.5$, Cantiello et al. (2009) found average convective velocities on the order of $1 - 10$km/s in the FeCZ, which our results for the models used here agree with. The model used for a direct comparison with Cantiello et al. (2009), with $t = 2.38 \times 10^6$yrs, shows similar values for $H_P = 0.22$ ($H_P = 0.24$ in Cantiello et al.) and $\langle v_c \rangle = 2.29$km/s, compared to $\langle v_c \rangle = 2.25$km/s in Cantiello et al. (2009). As there are differences in stellar radius and R_c, the models are not expected to give the same result, but they do fit qualitatively.

The models with $\alpha = 2$ already show significantly higher average convective velocities than those with $\alpha = 1.5$. This is both due to the convective velocities overall being higher, as determined in Sect. 4.2, and the range over which velocities are averaged being two pressure scale heights deep instead of just 1.5. In the model with $T_{eff} = 40$kK, $\langle v_c \rangle$ is already ~ 9km/s, which almost equals the highest values for models with $\alpha = 1.5$ on the late main sequence.

In the models with mixing-length parameters of $\alpha \geq 3$, most of the values for the convective velocities reach the local isothermal sound speed. For these large mixing-length parameters, the increases in average convective velocity stem mostly from the increase in αH_P. For the models with $\alpha = 30$, the convective velocities reach the sound speed always and at every grid point, as indicated by $M_c = 1$ at the upper boundary of the CZs, and convective velocities are averaged over the entire convection zone, causing $\langle v_c \rangle \approx$ const. . They are also always significantly higher than 10km/s, ranging from $\langle v_c \rangle = 27.4$km/s for $\alpha = 3$ at $T_{eff} = 40$kK to $\langle v_c \rangle = 47.6$km/s for $\alpha = 30$ at $T_{eff} = 25$kK.

According to Cantiello et al. (2009), $\sqrt{M_c \frac{\rho_c}{\rho_s}}$ should be on the order of 1 for models with well developed FeCZs. This is not the case for all of the models examined here. Generally, $\frac{\rho_c}{\rho_s}$ is on the order of $10^1 - 10^2$, increasing with decreasing T_{eff}. Most of the variation in $\sqrt{M_c \frac{\rho_c}{\rho_s}}$ is therefore caused by the isothermal Mach number M_c.

For the models of all mixing-length parameters except $\alpha = 0.5$ and $\alpha = 30$, the Mach number M_c increases with decreasing T_{eff}, as convective velocities at its upper boundary become larger. The upper boundary also moves to slightly lower temperatures with decreasing T_{eff}, as seen in Sect. 4.2, causing $c_{s,iso}$ to decrease. For $\alpha = 30$, $M_c = 1$ at all times, as the isothermal sound speed is reached immediately. For $\alpha = 0.5$, the Mach number actually decreases from $T_{eff} = 40$kK to $T_{eff} = 25$kK. Since the mixing length is so small for this mixing-length parameter, the convective velocities do not become much larger, with $\langle v_c \rangle$ only increasing by a factor of ~ 2. As a comparison, in models with $\alpha = 1.5$, where convective velocities within $1.5 H_P$ of the upper boundary are lower than the local sound speed as well, $\langle v_c \rangle$ increases by a factor of ~ 6 in the same temperature range. The FeCZ becomes more extended with decreasing temperatures, which is strongest for $\alpha = 0.5$ due to inflation (Sect. 4.2). This means that the highest convective velocities are reached further from its upper boundary, which causes v_c directly at the upper boundary to decrease with decreasing T_{eff}, even though v_c^{max} and $\langle v_c \rangle$ increase. This accounts for the lower Mach numbers at $T_{eff} = 25$kK for both the $60 M_\odot$ and $62 M_\odot$ models with $\alpha = 0.5$. The low Mach number leads to $\sqrt{M_c \frac{\rho_c}{\rho_s}} \sim 10^{-2}$ and an upper limit to v_s that is significantly lower than $\langle v_c \rangle$ with values on the order of 10^{-4}km/s. Compared to models with higher mixing-length parameters, the FeCZ for $\alpha = 0.5$ is therefore not well developed.

In the other models, $\sqrt{M_c \frac{\rho_c}{\rho_s}}$ increases with decreasing T_{eff} as both M_c as well as $\frac{\rho_c}{\rho_s}$ increase as convective motions in the FeCZ become stronger. For the models with $\alpha = 1.5$ and $\alpha = 2$, $\sqrt{M_c \frac{\rho_c}{\rho_s}}$ is low at $T_{eff} = 40$kK and reaches ~ 1 (order of magnitude) at $T_{eff} = 25$kK. In the models with $\alpha = 3$, it is on the order of 1 throughout the main sequence. For the considerably larger convective velocities in models with $\alpha = 5$ and $\alpha = 30$, $\sqrt{M_c \frac{\rho_c}{\rho_s}}$ exceeds the order of magnitude of 1 for the late main sequence at $T_{eff} = 15$kK. When it approaches or exceeds a value of 1, $v_s \leq \langle v_c \rangle \cdot \sqrt{M_c \frac{\rho_c}{\rho_s}}$ (Fig. 19) can reach high values, exceeding the isothermal sound speed at the surface of the stellar models. This is the case for the models with $\alpha = 2$ and 15kK, $\alpha = 3$ and 25kK as well as 15kK and at all temperatures for $\alpha = 5$ and $\alpha = 30$, including the HeCZ of the model with $\alpha = 30$ at 15kK.

5.2 Comparison with theoretical trends

Observational data regarding microturbulent velocities in massive stars is still scarce, especially for the stellar mass of $60 M_\odot$ discussed in this thesis. Nonetheless, Cantiello et al. (2009) found trends for the microturbulent velocities of stars with lower masses, which might still hold at the high mass of the stellar models examined here.

The data from Cantiello et al. (2009) suggests a key role of luminosity in microturbulence. Stars with a significant value for the microturbulent velocity (chosen as $\xi > 10$km/s due to uncertainties of ± 5km/s in the observations) are the most luminous ones in the samples. This dependence is found in the comparison of the stellar models with different mixing-length parameters as well. Models with the same effective temperature have higher luminosities for larger α (see Fig. 1) and they also show larger upper limits for the surface velocity amplitude (Table 4, Fig. 19). This is mainly related to the larger convective velocities in the upper region of the FeCZ in models with larger mixing-length parameters, as the model with $\alpha = 0.5$ and $62 M_\odot$ initial mass has higher luminosities than some models with larger mixing-length parameters, while the convective velocities and v_s are nonetheless much lower. In fact, the comparison

between the $60M_\odot$ and $62M_\odot$ models with $\alpha = 0.5$ shows no significant differences for either $\langle v_c \rangle$ or v_s.

Cantiello et al. (2009) also identified $\langle v_c \rangle = 2.5$km/s as a critical value for causing microturbulence. This threshold is not reached for models with $\alpha = 0.5$, therefore there should be no observable microturbulence. The surface velocity amplitudes confirm the prediction, as they are on the order of 10^{-4}km/s. For models with $\alpha = 1.5$, we have $\langle v_c \rangle = 1.19$km/s at $T_{\rm eff} = 40$kK, with $v_s \sim 10^{-1}$km/s, while the model with $T_{\rm eff} = 25$kK exceeds the critical value with $\langle v_c \rangle = 7.44$km/s. The surface velocity in this model is significant with $v_s = 2.07$km/s, but below the detection threshold of $\xi > 10$km/s determined in Cantiello et al. (2009). In the late main sequence model with $T_{\rm eff} = 15$kK, the surface velocity reaches $v_s = 7.65$km/s, which is still below the threshold. However, these velocities are both within the range of observed microturbulent velocities, which are about $0 - 20$km/s in hot massive stars and high enough to be potentially observable. Consequently, assuming a mixing-length parameter of $\alpha = 1.5$, microturbulence should not be present for $60M_\odot$ stars early on the main sequence, but arise during the main sequence evolution.

For models with $\alpha \geq 2$, the critical average velocity is exceeded throughout the main sequence evolution, therefore microturbulence should be observable with sufficient data if stars have mixing-length parameters that large. Important to note is the fact that in all examined models where $v_s > 10$km/s, the surface velocity amplitude also exceeds the isothermal sound speed on the surface (see Table 3) as well as the range of observed microturbulent velocities. For the models with $\alpha = 5$ and $\alpha = 30$ this is the case for all examined main sequence models.

Assuming sub-surface convection is in fact the cause of microturbulence (Cantiello et al. 2009), the results rule out the mixing-length parameter $\alpha = 0.5$ as a realistic value in massive stars, since convection in these models can not trigger the observed microturbulence. If $\xi \approx 20$km/s holds as an upper approximate upper limit for the microturbulent velocities even at higher stellar masses, it also rules out mixing-length parameters of $\alpha \geq 5$, as v_s exceeds the observations for ξ by a significant amount for all examined models throughout the main sequence. In models with $\alpha = 3$, observed microturbulent velocities are significantly exceeded both for the model with $T_{\rm eff} = 25$kK and with $T_{\rm eff} = 15$kK, ruling this mixing-length parameter out as well. The models with $\alpha = 2$ seem to be a borderline case, where microturbulence is present throughout the main sequence evolution, only exceeding $v_s > 20$km/s in the model with $T_{\rm eff} = 15$kK. Due to the low amount of observational data, meaning $\xi \sim 20$km/s is not a strong upper limit for microturbulent velocities, $\alpha = 2$ does not clearly disagree with observations and can be regarded as a rough upper limit for the mixing-length parameter.

6 Conclusion

In this thesis, a one-dimensional hydrodynamical stellar evolution code was used to investigate the properties of convective zones in the outer envelopes of massive stars, specifically stars with an initial mass of $60M_{\odot}$ and solar initial composition, as a function of the mixing-length parameter. The computations were done with the same physics and assumptions as Brott et al. (2011).

It was shown that the mixing-length parameter significantly influences envelope inflation as well as macro- and microturbulence. Models with larger mixing-length parameters have larger convective velocities, caused by the increased turbulent pressure. This leads to less inflated envelopes, as more energy can be transported through convective motions. The convective velocities also reach the local isothermal sound speed more often and throughout greater parts of the FeCZ the larger the mixing-length parameter is. Larger α also lead to increased convective velocities in the upper part of the FeCZ, causing stronger surface velocity amplitudes, which are connected to microturbulence.

The comparisons with observations for macroturbulent velocities (Simón-Díaz 2015) and trends found for microturbulence (Cantiello et al. 2009) showed that the models with mixing-length parameters of $\alpha = 0.5$ and $\alpha \geq 3$ can not explain the observational data. The model with $\alpha = 2$ was established as a borderline case for both macroturbulence and microturbulence, where models with a larger mixing-length parameter show significantly different behaviour compared to models with small mixing-length parameters. Regarding the difference between the mixing-length parameters of $\alpha = 1.5$ and $\alpha = 2$, no definite judgement can be made. For the range between $\alpha \geq 0.5$ and $\alpha = 2$, more models with different mixing-length parameters and initial masses would need to be computed, combined with analysing a greater amount of observational data in order to sufficiently calibrate the mixing-length parameter. Including the turbulence terms into the stellar code (see Grassitelli et al. 2015) for more accurate models might also be necessary to draw further conclusions.

References

[1] Böhm-Vitense, E. 1958, ZAp, 46, 108

[2] Brott, I., de Mink, S. E., Cantiello, M., et al. 2011, arXiv:1102.0530v2 [astro-ph.SR]

[3] Cantiello, M., Langer, N., Brott, I., et al., 2009, arXiv:0903.2049v1

[4] Grassitelli L., Fossati L., Simón-Díaz S., et. al., 2015, arXiv:1507.03988v1 [astro-ph.SR]

[5] Iglesias, C. A., Rogers, F. J., & Wilson, B. G. 1992, ApJ, 397, 717

[6] Iglesias, C. A. & Rogers, F. J. 1996, ApJ, 464, 943

[7] Langer, N. & Kudritzki, R. P. 2014, arXiv:1403.2212v1 [astro-ph.SR]

[8] Pols, E. R. (2009). Stellar Structure and Evolution.

[9] Sanyal D., Grassitelli, L., Langer, N., & Bestenlehner, J. M. 2015, arXiv:1506.02997v1 [astro-ph.SR]

[10] Simón-Díaz, S. 2015, in IAU Symposium, Vol. 307, IAU Symposium, 194–199

[11] Vink, J. S., de Koter, A., & Lamers, H. J. G. L. M. 2001, A&A, 369, 574

7 Appendix

7.1 Macroturbulence

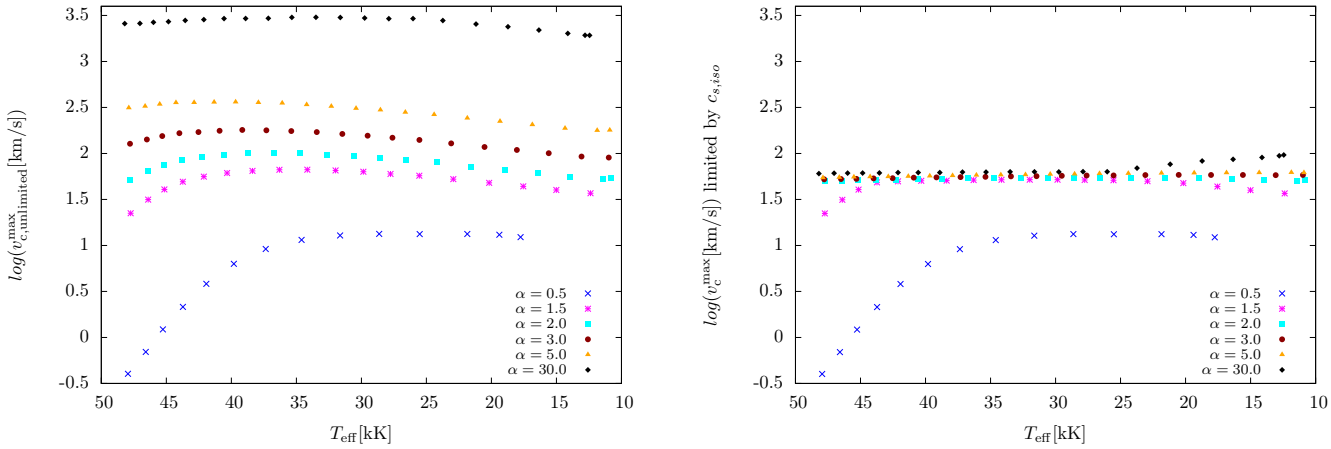

Figure 20: Maximum convective velocities on a log scale in the sets of stellar models with different mixing-length parameters. The model with $\alpha = 0.5$ has an initial mass of $62M_{\odot}$, the models with higher mixing-length parameters have initial masses of $60M_{\odot}$. Left panel: Maximum convective velocities without applying the limitation of Eq. 10. These values have to be regarded as non-realistic, as the the convective velocity often exceeds the local isothermal sound speed. Right panel: Same as left, but with the limitation for v_{c}.

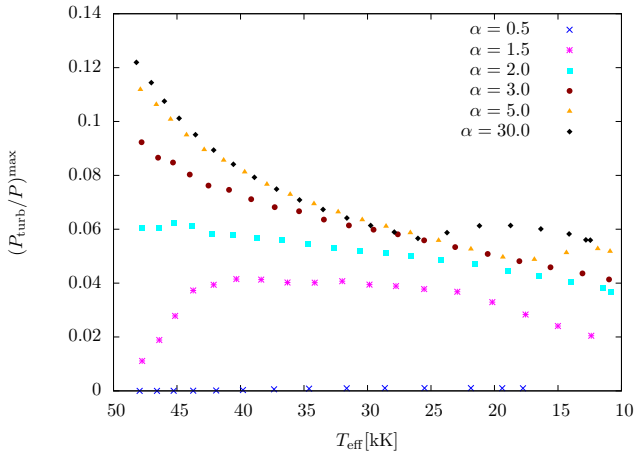

Figure 21: The maximum turbulent pressure fraction, calculated using Eq. 5, as a function of T_{eff} for the model with $62M_{\odot}$ initial mass with $\alpha = 0.5$ and the models with $60M_{\odot}$ and with a set of different mixing-length parameters. See Fig. 12 for log scale in order to distinguish $(P_{\mathrm{turb}}/P)^{\mathrm{max}}$ for $\alpha = 0.5$ from zero.

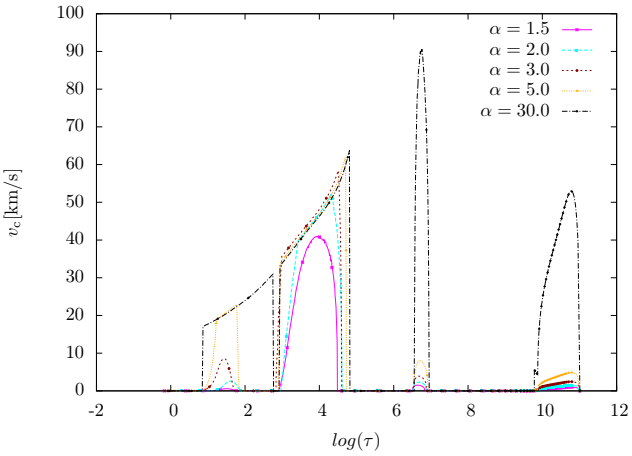

Figure 22: Convective velocity in the stellar models with $T_{\mathrm{eff}} = 15\mathrm{kK}$, initial mass $60M_{\odot}$ and with different mixing-length parameter, as a function of the optical depth as $log(\tau)$. Visible are several peaks in v_{c}, in the order of increasing $log(\tau)$, caused by the helium opacity peak at $log(T) \approx 4.6$, the iron opacity peak at $log(T) \approx 5.3$, the second iron opacity peak at $log(T) \approx 6.2$ and the convective core. For models with all mixing-length parameters except $\alpha = 30$, where $v_{\mathrm{c}}^{\mathrm{max}}$ occurs in the CZ caused by the second iron opacity peak, the maximum convective velocities occur in the FeCZ.

7.1.1 Properties as a function of optical depth

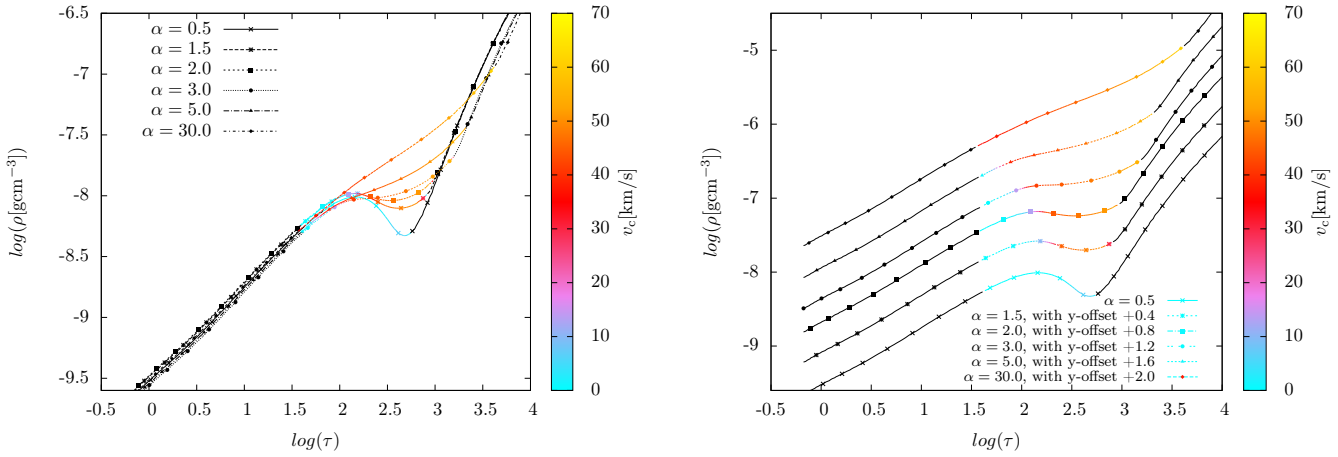

Figure 23: Left panel: Convective velocity (colour-coded) in the outer envelope as a function of density and optical depth for stellar models with $T_{\rm eff} \approx 40$kK and different mixing-length parameters. Regions without convection are coloured black. Right panel: Same as left panel, but with an incremental offset in $log(\rho)$ in order to distinguish the tracks for different models better.

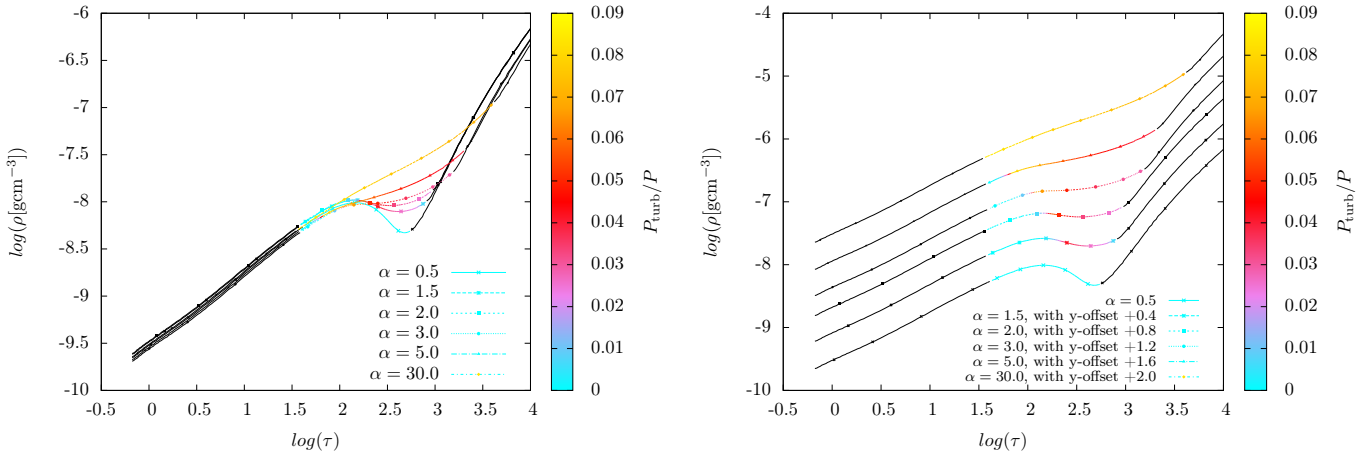

Figure 24: Left panel: The turbulent pressure fraction (colour-coded) in the outer envelope of stellar models with $T_{\rm eff} \approx 40$kK and different mixing-length parameters as a function of density and optical depth. Regions without convection are coloured black. Right panel: Same as left panel, but with an incremental offset for $log(\rho)$.

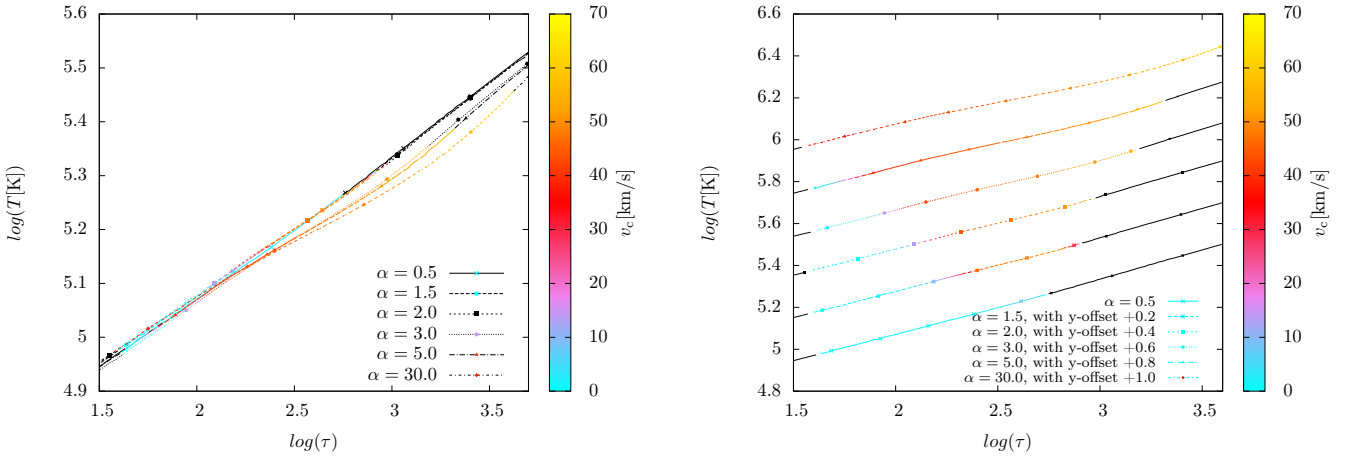

Figure 25: Left panel: Convective velocity (colour-coded) in the outer envelope of stellar models with $T_{\rm eff} \approx 40$kK and different mixing-length parameters as a function of temperature and optical depth. Shown is the range of the FeCZ, regions without convection are coloured black. Right panel: Same as left panel, but with an incremental offset for $log(T)$.

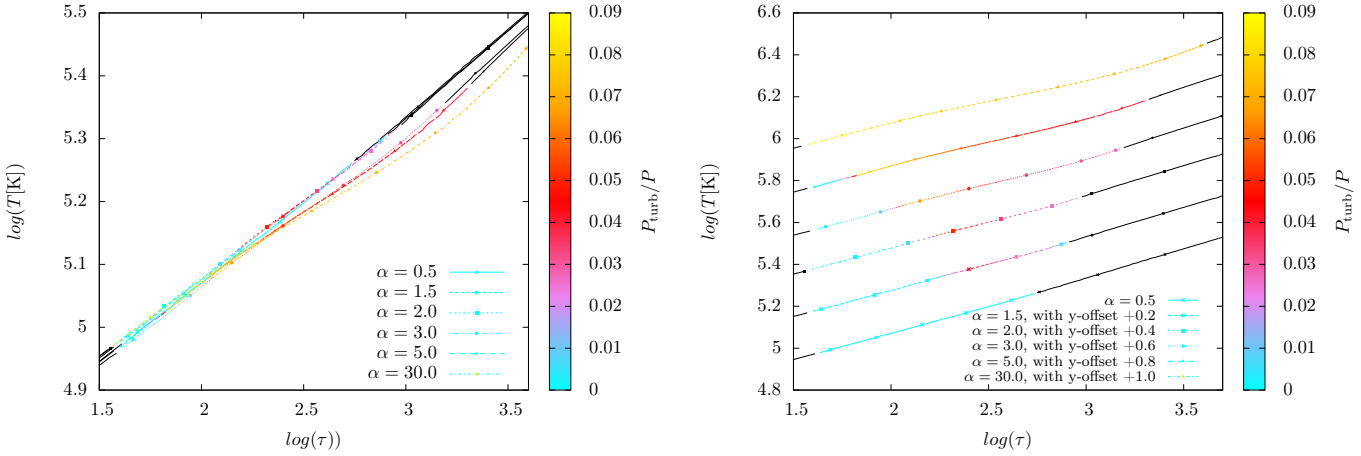

Figure 26: Left panel: The turbulent pressure fraction (colour-coded) in the outer envelope of stellar models with $T_{\rm eff} \approx 40$kK and different mixing-length parameters as a function of temperature and optical depth, showing the range of the FeCZ. Regions without convection are coloured black. Right panel: Same as left panel, but with an incremental offset for $log(T)$.

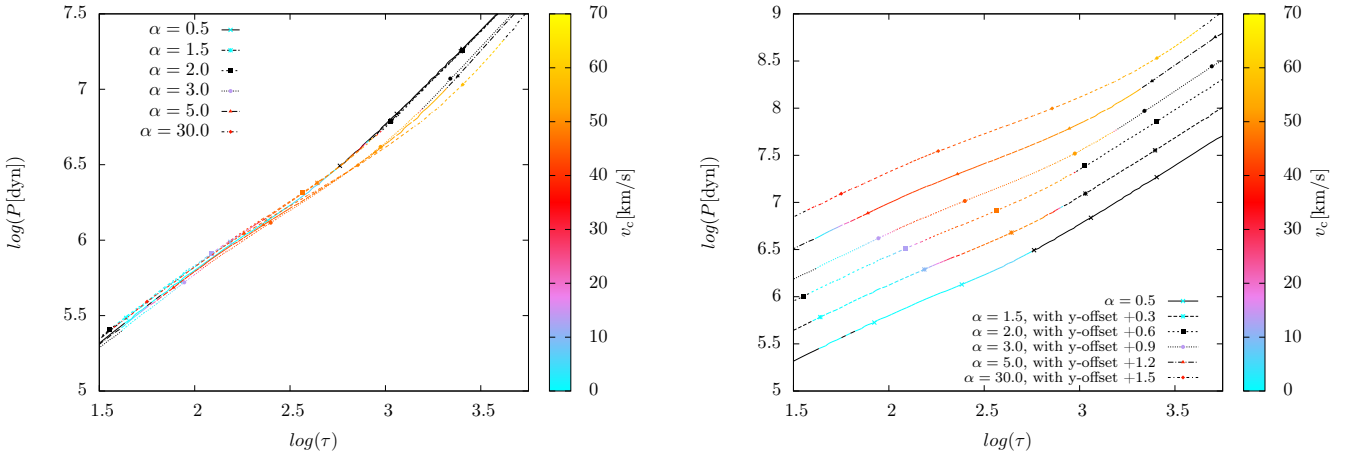

Figure 27: Left panel: Convective velocity (colour-coded) in the outer envelope of stellar models with $T_{\rm eff} \approx 40$kK and different mixing-length parameters as a function of total pressure P and optical depth. Regions without convection are coloured black, shown is the range of the FeCZ. Right panel: Same as left panel, but with an incremental offset for $log(T)$.

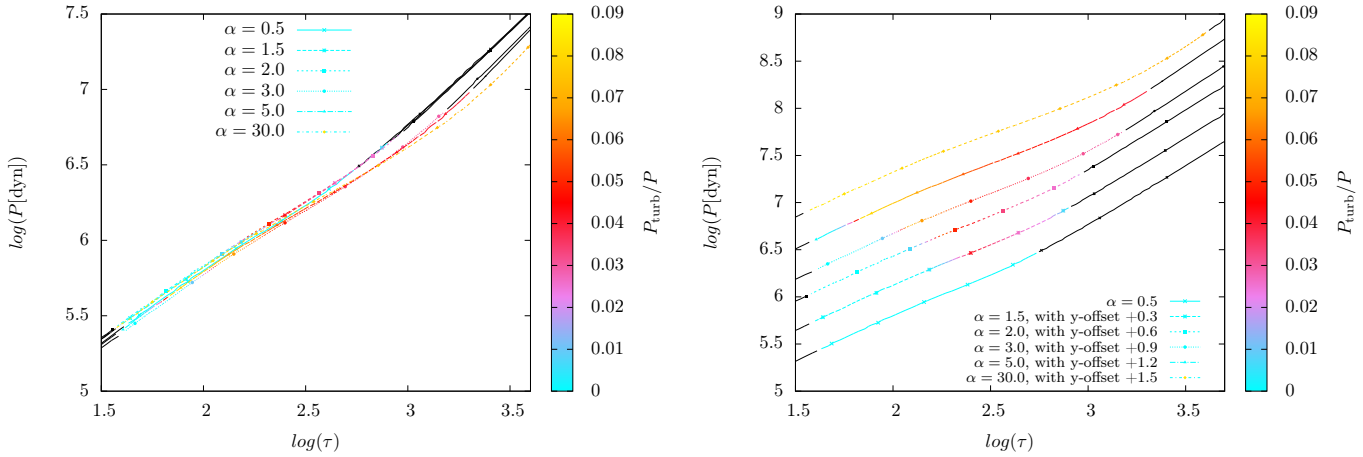

Figure 28: Left panel: The turbulent pressure fraction (colour-coded) in the outer envelope of stellar models with $T_{\rm eff} \approx 40$kK and different mixing-length parameters as a function of total pressure and optical depth, showing the range of the FeCZ. Regions without convection are coloured black. Right panel: Same as left panel, but with an incremental offset for $log(P)$.

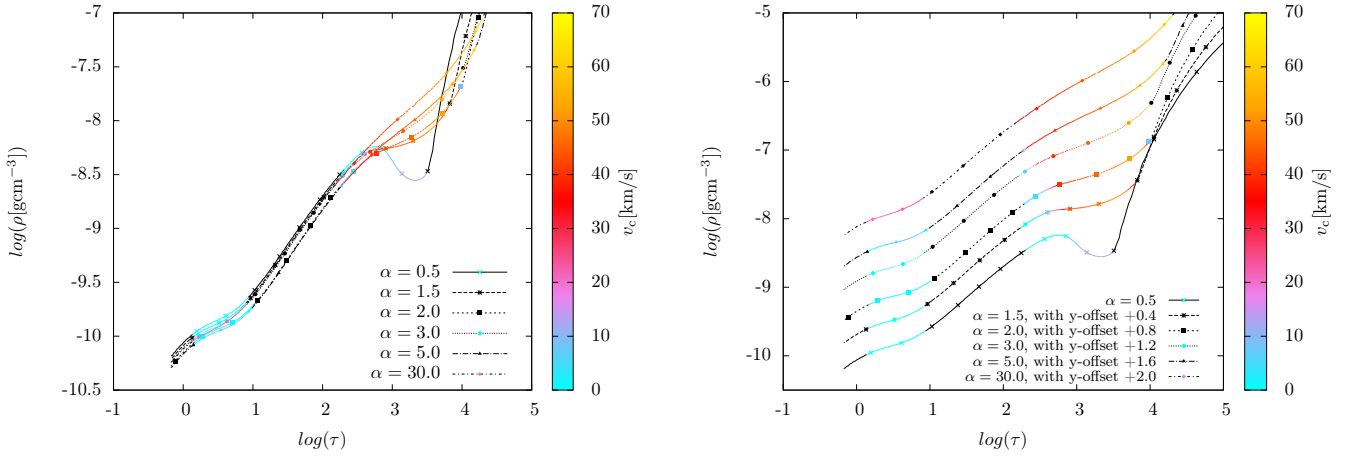

Figure 29: Left panel: Convective velocity (colour-coded) in the outer envelope of stellar models with $T_{\rm eff} \approx 25$kK and different mixing-length parameters as a function of density and optical depth. Shown are both the HeCZ and the FeCZ, regions without convection are coloured black. Right panel: Same as left panel, but with an incremental offset for $log(\rho)$.

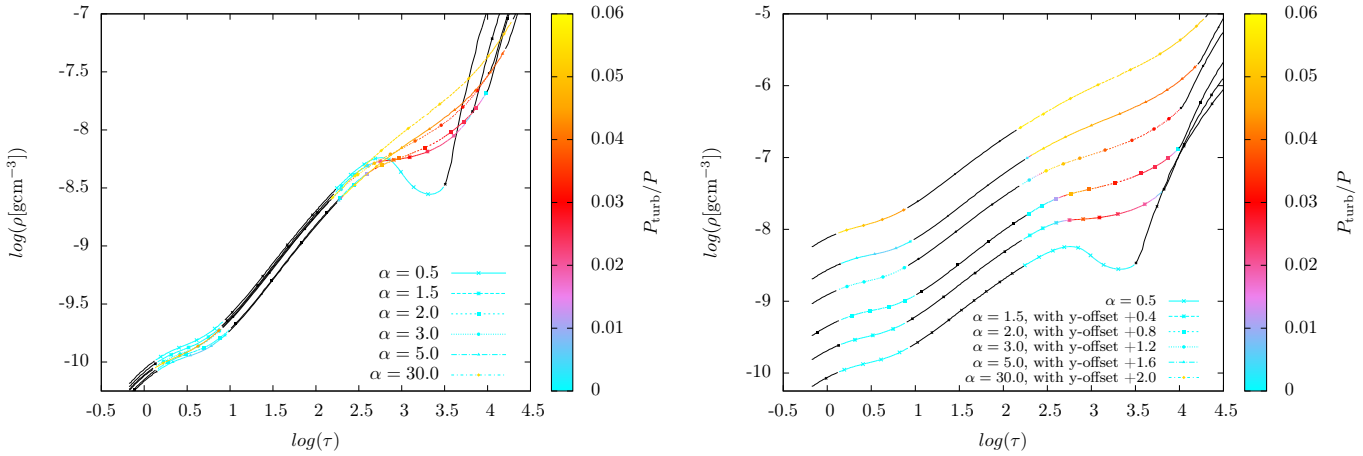

Figure 30: Left panel: The turbulent pressure fraction (colour-coded) in the outer envelope of stellar models with $T_{\rm eff} \approx 25$kK and different mixing-length parameters as a function of density and optical depth. Shown are both the HeCZ and the FeCZ, regions without convection are coloured black. Right panel: Same as left panel, but with an incremental offset for $log(\rho)$.

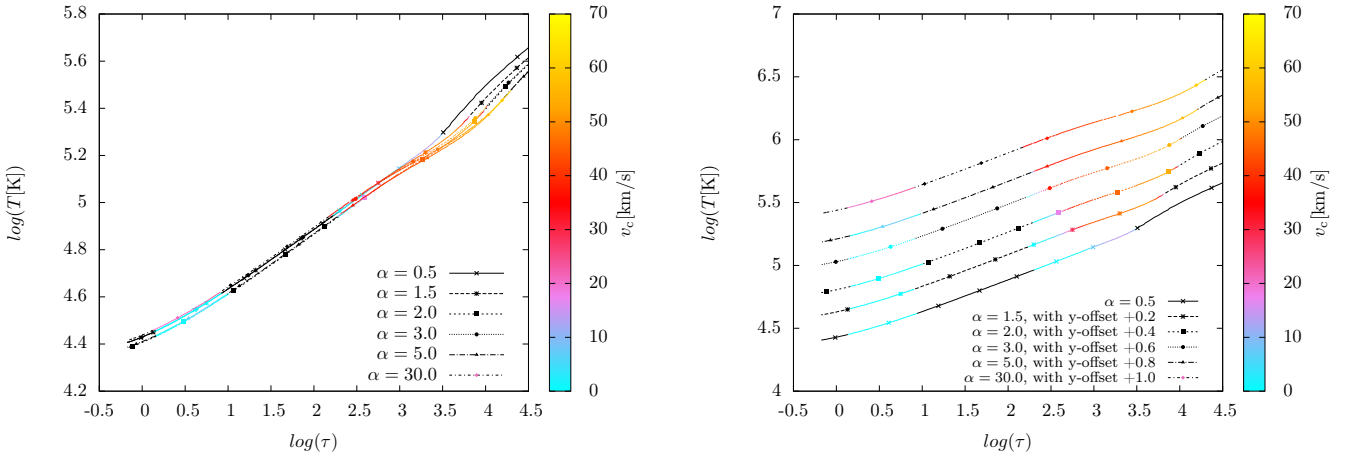

Figure 31: Left panel: Convective velocity (colour-coded) in the outer envelope of stellar models with $T_{\rm eff} \approx 25$kK and different mixing-length parameters as a function of temperature and optical depth. Shown are both the HeCZ and the FeCZ, regions without convection are coloured black. Right panel: Same as left panel, but with an incremental offset for $log(T)$.

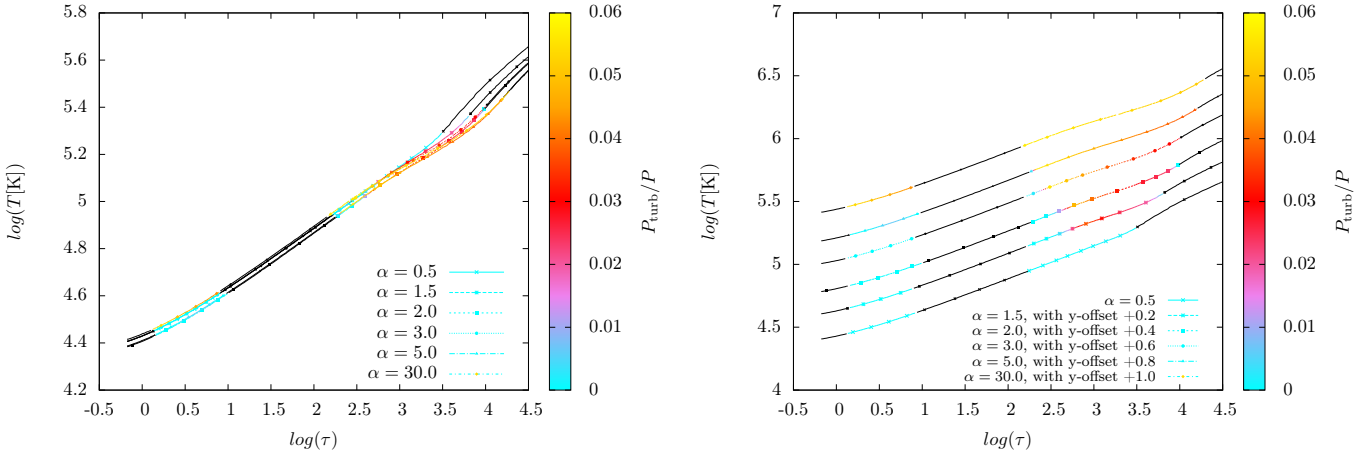

Figure 32: Left panel: The turbulent pressure fraction (colour-coded) in the outer envelope of stellar models with $T_{\rm eff} \approx 25$kK and different mixing-length parameters as a function of temperature and optical depth. Shown are both the HeCZ and the FeCZ, regions without convection are coloured black. Right panel: Same as left panel, but with an incremental offset for $log(T)$.

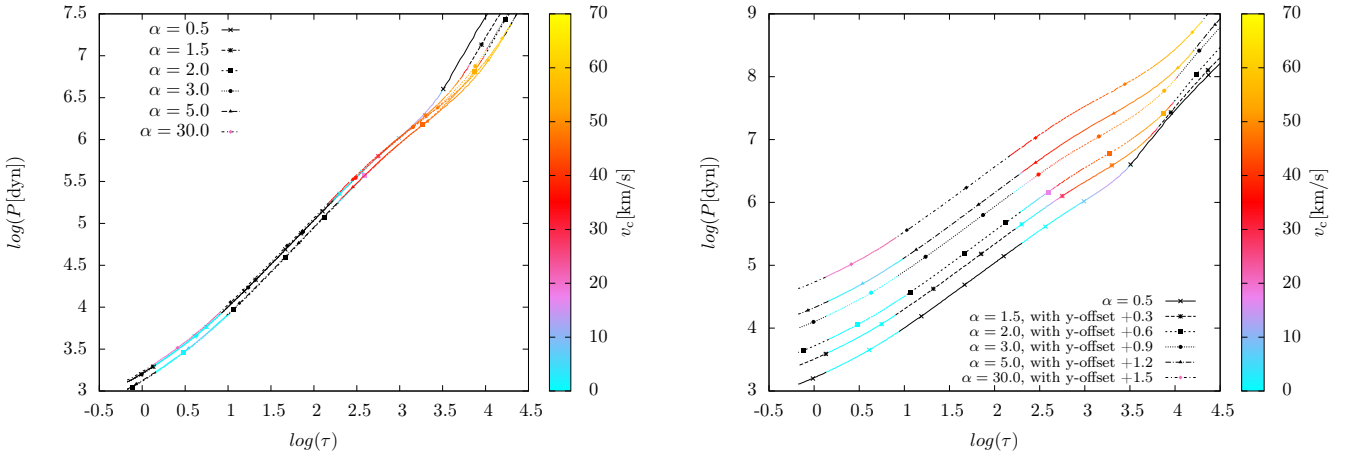

Figure 33: Left panel: Convective velocity (colour-coded) in the outer envelope of stellar models with $T_{\rm eff} \approx 25$kK and different mixing-length parameters as a function of total pressure and optical depth. Shown are both the HeCZ and the FeCZ, regions without convection are coloured black. Right panel: Same as left panel, but with an incremental offset for $log(P)$.

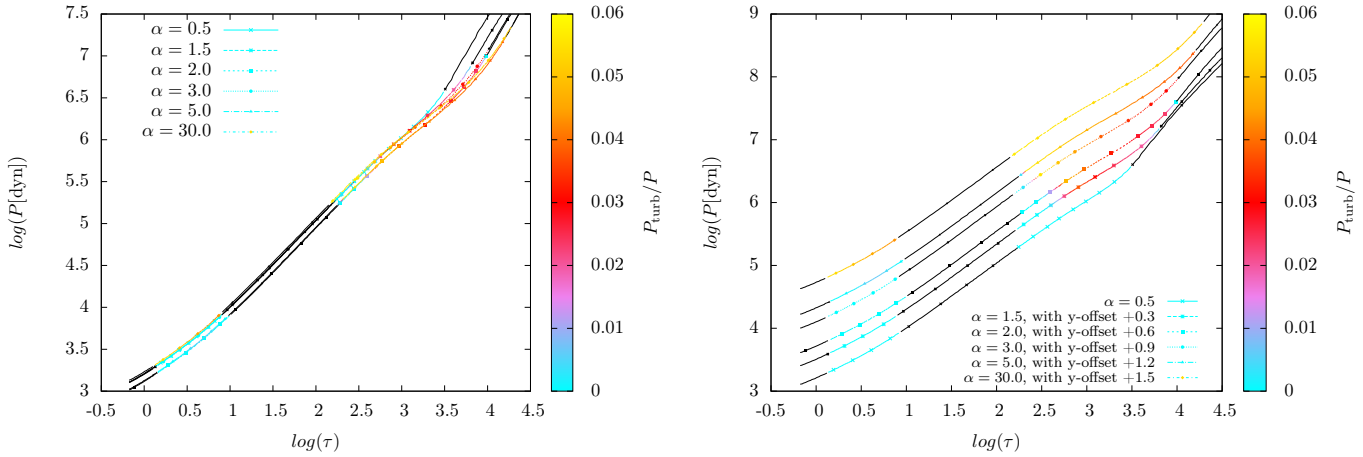

Figure 34: Left panel: The turbulent pressure fraction (colour-coded) in the outer envelope of stellar models with $T_{\rm eff} \approx 25$kK and different mixing-length parameters as a function of total pressure and optical depth. Shown are both the HeCZ and the FeCZ, regions without convection are coloured black. Right panel: Same as left panel, but with an incremental offset for $log(P)$.

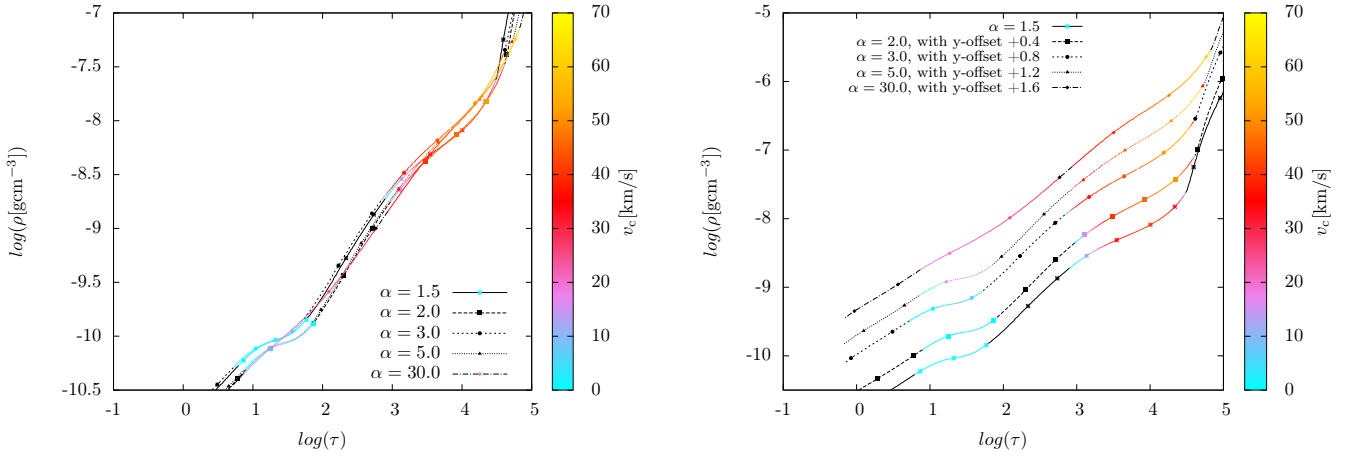

Figure 35: Left panel: Convective velocity (colour-coded) in the outer envelope of stellar models with $T_{\rm eff} \approx 15$kK and different mixing-length parameters as a function of density and optical depth. Shown are both the HeCZ and the FeCZ, regions without convection are coloured black. Right panel: Same as left panel, but with an incremental offset for $log(\rho)$.

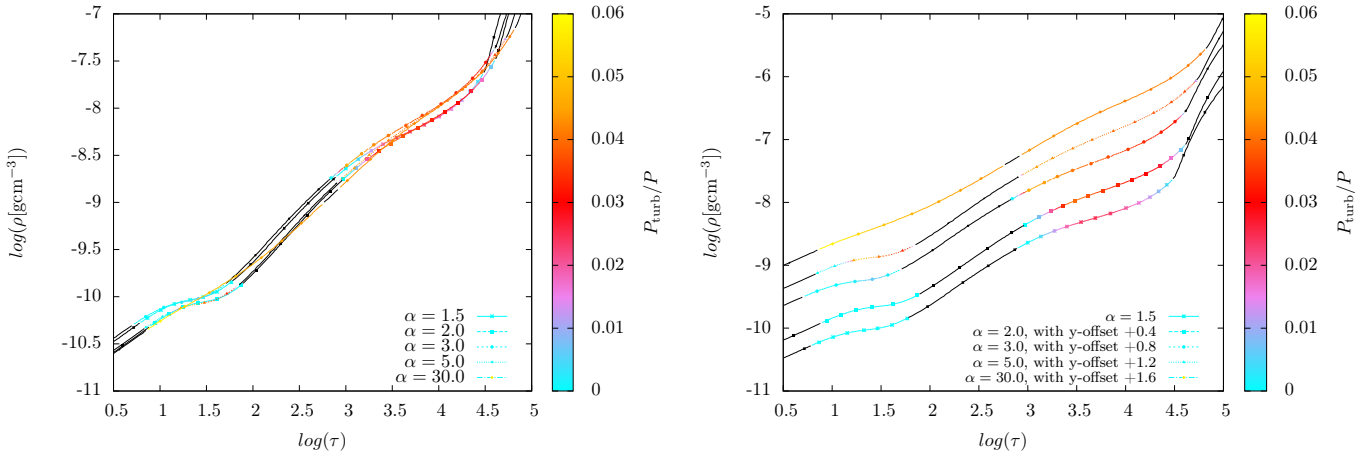

Figure 36: Left panel: The turbulent pressure fraction (colour-coded) in the outer envelope of stellar models with $T_{\rm eff} \approx 15$kK and different mixing-length parameters as a function of density and optical depth. Shown are both the HeCZ and the FeCZ, regions without convection are coloured black. Right panel: Same as left panel, but with an incremental offset for $log(\rho)$.

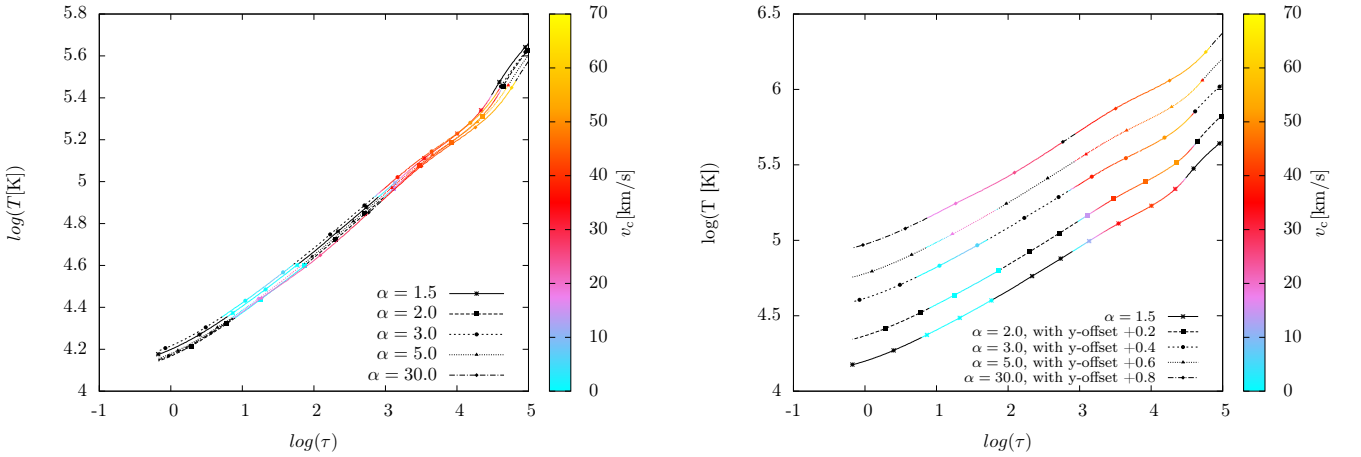

Figure 37: Left panel: Convective velocity (colour-coded) in the outer envelope of stellar models with $T_{\rm eff} \approx 15$kK and different mixing-length parameters as a function of temperature and optical depth. Shown are both the HeCZ and the FeCZ, regions without convection are coloured black. Right panel: Same as left panel, but with an incremental offset for $log(T)$.

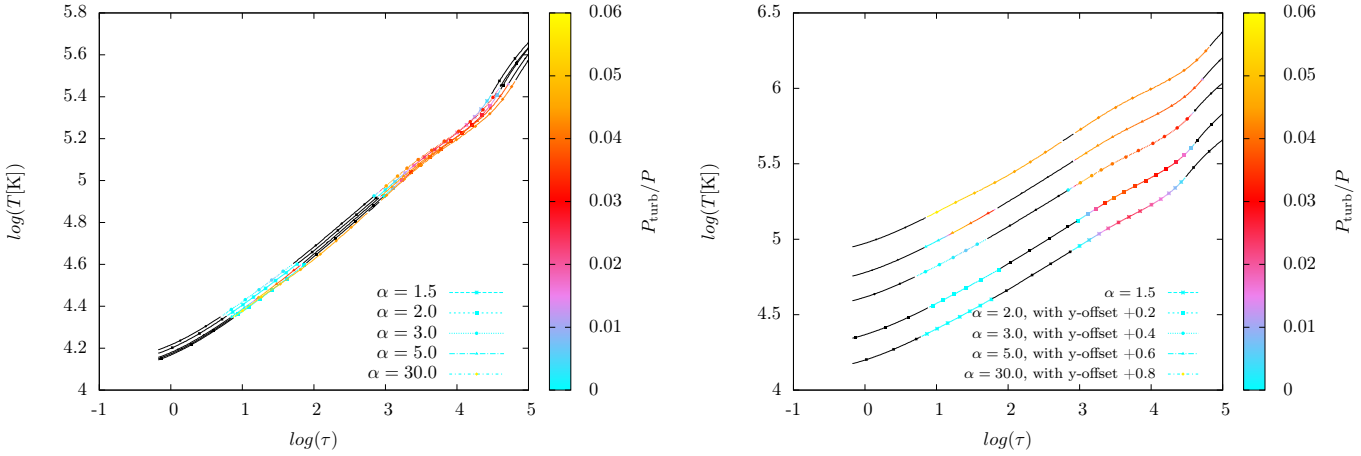

Figure 38: Left panel: The turbulent pressure fraction (colour-coded) in the outer envelope of stellar models with $T_{\rm eff} \approx 15$kK and different mixing-length parameters as a function of temperature and optical depth. Shown are both the HeCZ and the FeCZ, regions without convection are coloured black. Right panel: Same as left panel, but with an incremental offset for $log(T)$.

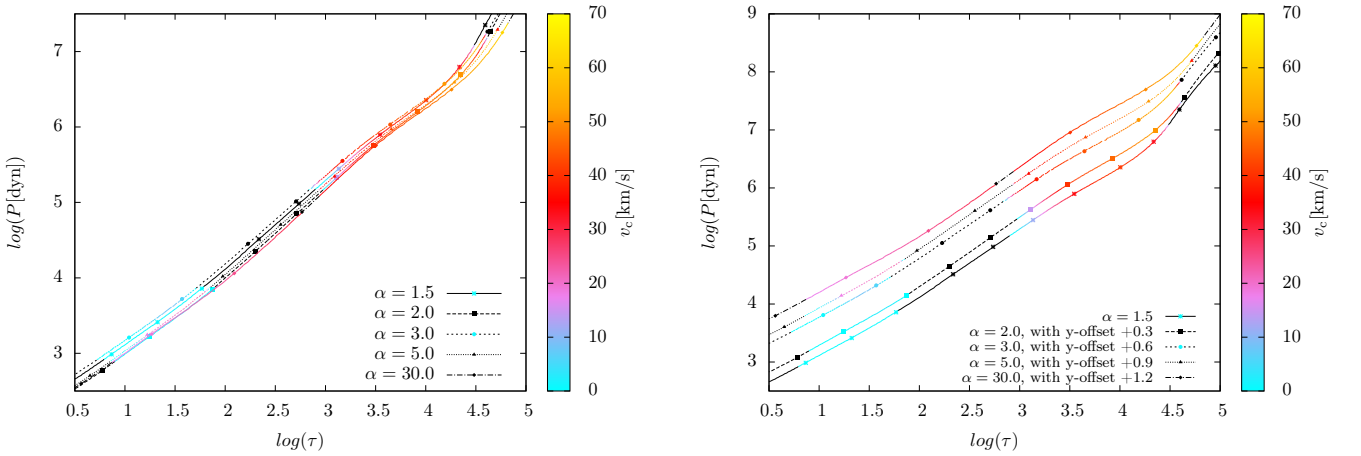

Figure 39: Left panel: Convective velocity (colour-coded) in the outer envelope of stellar models with $T_{\rm eff} \approx 15$kK and different mixing-length parameters as a function of total pressure and optical depth. Shown are both the HeCZ and the FeCZ, regions without convection are coloured black. Right panel: Same as left panel, but with an incremental offset for $log(P)$.

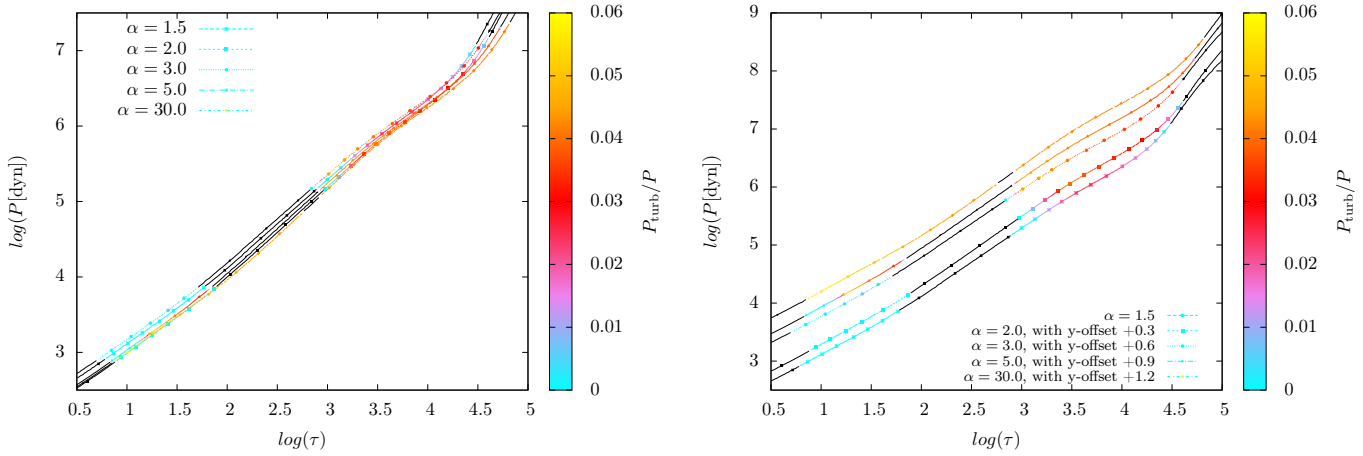

Figure 40: Left panel: The turbulent pressure fraction (colour-coded) in the outer envelope of stellar models with $T_{\rm eff} \approx 15$kK and different mixing-length parameters as a function of total pressure and optical depth. Shown are both the HeCZ and the FeCZ, regions without convection are coloured black. Right panel: Same as left panel, but with an incremental offset for $log(P)$.

7.2 Microturbulence

Table 3: Comparison between the upper limit for the surface velocity $v_{\rm s}$ (see Table 4) and the isothermal sound speed on the stellar surface for stellar models with different mixing-length parameters and effective temperatures

Model	$v_{\rm s}[cm/s]$	$c_{\rm s,iso}^{\rm surface}$[cm/s]
$60M_{\odot}, \alpha = 0.5$, 40kK	2.81E+01	2.36E+06
$60M_{\odot}, \alpha = 0.5$, 25kK	2.88E+01	1.80E+06
$62M_{\odot}, \alpha = 0.5$, 40kK	2.38E+01	2.33E+06
$62M_{\odot}, \alpha = 0.5$, 25kK	3.17E+01	1.83E+06
$60M_{\odot}, \alpha = 1.5$, 40kK	7.39E+03	2.35E+06
$60M_{\odot}, \alpha = 1.5$, 25kK	2.07E+05	1.83E+06
$60M_{\odot}, \alpha = 1.5$, 15kK	7.65E+05	1.40E+06
$60M_{\odot}, \alpha = 2.0$, 40kK	7.46E+04	2.35E+06
$60M_{\odot}, \alpha = 2.0$, 25kK	5.29E+05	1.78E+06
$60M_{\odot}, \alpha = 2.0$, 15kK	5.83E+06	1.35E+06
$60M_{\odot}, \alpha = 3.0$, 40kK	5.10E+05	2.31E+06
$60M_{\odot}, \alpha = 3.0$, 25kK	2.71E+06	1.83E+06
$60M_{\odot}, \alpha = 3.0$, 15kK	7.06E+06	1.43E+06
$60M_{\odot}, \alpha = 5.0$, 40kK	3.42E+06	2.33E+06
$60M_{\odot}, \alpha = 5.0$, 25kK	1.47E+07	1.79E+06
$60M_{\odot}, \alpha = 5.0$, 15kK	4.56E+07	1.37E+06
$60M_{\odot}, \alpha = 30.0$, 40kK	2.25E+07	2.35E+06
$60M_{\odot}, \alpha = 30.0$, 25kK	3.15E+07	1.85E+06
$60M_{\odot}, \alpha = 30.0$, 15kK	6.08E+07	1.36E+06
$60M_{\odot}, \alpha = 30.0$, 15kK (HeCZ)	5.29E+06	1.36E+06
$60M_{\odot}, \alpha = 1.5, t = 2.38 \times 10^6 yrs$	1.82E+04	2.22E+06

Table 4: Properties and results for stellar models with different mixing-length parameters and effective temperatures. Shown are the radius of the upper boundary of the FeCZ R_c; the pressure scale height H_P at the upper boundary; the radius when R_c is decreased by one mixing length, $R_c - \alpha \cdot H_P$; the average convective velocity $\langle v_c \rangle$; the isothermal Mach number M_c at the upper boundary of the FeCZ; the density at the upper boundary of the FeCZ ρ_c; the surface density ρ_s; the value $\sqrt{M_c \cdot \frac{\rho_c}{\rho_s}}$; and the upper limit for the surface velocity v_s, given by $\langle v_c \rangle \cdot \sqrt{M_c \cdot \frac{\rho_c}{\rho_s}}$. For a stellar model with $\alpha = 30$ and $T_{\rm eff} \approx 15$kK, these values were also calculated for the HeCZ.

Model	R_c [cm]	α	$H_P(R_c)$ [cm]	$R_c - \alpha \cdot H_P$ [cm]	$\langle v_c \rangle$ [cm/s]	M_c	ρ_c[gcm^{-3}]	ρ_s[gcm^{-3}]	$\sqrt{M_c \cdot \frac{\rho_c}{\rho_s}}$	$\langle v_c \rangle \cdot \sqrt{M_c \cdot \frac{\rho_c}{\rho_s}}$[cm/s]
$60M_\odot, \alpha = 0.5, 40kK$	1.09E+12	0.5	7.91E+09	1.09E+12	4.34E+02	1.67E-04	6.53E-09	2.61E-10	6.48E-02	2.81E+01
$60M_\odot, \alpha = 0.5, 25kK$	3.08E+12	0.5	8.43E+10	3.04E+12	8.06E+02	2.50E-05	3.18E-09	6.19E-11	3.58E-02	2.88E+01
$62M_\odot, \alpha = 0.5, 40kK$	1.19E+12	0.5	9.50E+09	1.19E+12	4.12E+02	1.32E-04	5.62E-09	2.22E-10	5.77E-02	2.38E+01
$62M_\odot, \alpha = 0.5, 25kK$	2.94E+12	0.5	7.53E+10	2.90E+12	7.81E+02	3.40E-05	3.16E-09	6.53E-11	4.06E-02	3.17E+01
$60M_\odot, \alpha = 1.5, 40kK$	1.13E+12	1.5	8.42E+09	1.12E+12	1.19E+05	1.64E-04	5.71E-09	2.42E-10	6.23E-02	7.39E+03
$\alpha = 1.5, 25kK$	2.89E+12	1.5	7.99E+10	2.77E+12	7.44E+05	1.65E-03	2.90E-09	6.14E-11	2.79E-01	2.07E+05
$\alpha = 1.5, 15kK$	6.65E+12	1.5	5.56E+11	5.81E+12	1.31E+06	2.04E-03	1.89E-09	1.14E-11	5.82E-01	7.65E+05
$\alpha = 2.0, 40kK$	1.12E+12	2.0	8.22E+09	1.10E+12	9.16E+05	2.88E-04	5.66E-09	2.46E-10	8.15E-02	7.46E+04
$\alpha = 2.0, 25kK$	3.19E+12	2.0	1.02E+11	2.99E+12	1.95E+06	1.50E-03	2.60E-09	5.28E-11	2.72E-01	5.29E+05
$\alpha = 2.0, 15kK$	7.24E+12	2.0	6.93E+11	5.85E+12	2.80E+06	2.20E-02	1.77E-09	8.93E-12	2.08E+00	5.83E+06
$\alpha = 3.0, 40kK$	1.22E+12	3.0	1.03E+10	1.19E+12	2.74E+06	1.42E-03	4.99E-09	2.04E-10	1.86E-01	5.10E+05
$\alpha = 3.0, 25kK$	2.91E+12	3.0	8.38E+10	2.66E+12	3.33E+06	1.47E-02	2.63E-09	5.84E-11	8.13E-01	2.71E+06
$\alpha = 3.0, 15kK$	6.28E+12	3.0	5.13E+11	4.74E+12	3.73E+06	2.45E-02	1.80E-09	1.23E-11	1.89E+00	7.06E+06
$\alpha = 5.0, 40kK$	1.19E+12	5.0	9.87E+09	1.14E+12	3.83E+06	3.33E-02	5.08E-09	2.12E-10	8.93E-01	3.42E+06
$\alpha = 5.0, 25kK$	3.15E+12	5.0	1.05E+11	2.63E+12	4.15E+06	2.62E-01	2.46E-09	5.11E-11	3.55E+00	1.47E+07
$\alpha = 5.0, 15kK$	6.95E+12	5.0	6.55E+11	3.67E+12	4.49E+06	5.83E-01	1.66E-09	9.39E-12	1.02E+01	4.56E+07
$\alpha = 30.0, 40kK$	1.14E+12	30.0	9.07E+09	1.06E+12	4.75E+06	1.00E+00	5.09E-09	2.28E-10	4.73E+00	2.25E+07
$\alpha = 30.0, 25kK$	2.82E+12	30.0	8.25E+10	2.17E+12	4.76E+06	1.00E+00	2.51E-09	5.73E-11	6.62E+00	3.15E+07
$\alpha = 30.0, 15kK$	7.48E+12	30.0	7.58E+11	3.49E+12	4.73E+06	1.00E+00	1.45E-09	8.76E-12	1.29E+01	6.08E+07
$\alpha = 30.0, 15kK$ (HeCZ)	1.03E+13	30.0	2.87E+11	7.89E+12	2.33E+06	1.00E+00	4.52E-11	8.76E-12	2.27E+00	5.29E+06
$\alpha = 1.5, t = 2.38 \times 10^6 yrs$	1.43E+12	1.5	1.52E+10	1.41E+12	2.29E+05	2.12E-04	4.51E-09	1.51E-10	7.95E-02	1.82E+04

Erklärung:
Ich versichere, dass ich diese Arbeit selbständig verfasst und keine anderen als die angegebenen Quellen und Hilfsmittel benutzt sowie die Zitate kenntlich gemacht habe.

Bonn, den ....

Datum Unterschrift